MICROFLUIDIC PLASMONIC PACKED-BED REACTOR (μPPBR) FOR PHOTOCATALYTIC WATER PURIFICATION

YEUNG PUI HONG

MPhil

The Hong Kong Polytechnic University

2019

The Hong Kong Polytechnic University

Department of Applied Physics

Microfluidic plasmonic packed-bed reactor (μPPBR) for photocatalytic water purification

YEUNG Pui Hong

A thesis submitted in partial fulfillment of the requirements for the degree of Master of Philosophy

June 2018

CERTIFICATE OF ORIGINALITY

I hereby declare that this thesis is my own work and that, to the best of my knowledge and belief, it reproduces no material previously published or written, nor material that has been accepted for the award of any other degree or diploma, except where due acknowledgement has been made in the text.

_____(Signed)

Yeung Pui Hong_____(Name of the student)

Abstract

This M.Phil. study reports a novel microfluidic plasmonic packed-bed reactor (μPPBR) that is filled with Au-decorated TiO_2 microspheres with the aims to sensitize TiO_2 to visible light using localized surface plasmonic resonance (LSPR) and to also enhance the mass transfer inside the microfluidic reactor for high efficiency. Photodegradation of organic pollutants using sunlight has long been regarded as the idea technique for water decontamination, but the widely-used TiO_2 material is not responsive to visible light. Although different microfluidic reactors have been developed to study the reaction kinetics, their degradation efficiency in one-pass operation is often limited by the low mass transfer. To overcome these problems, this research stuffs Au/TiO_2 microspheres into a microchamber to form the μPPBR. The novelty of this work lies in the combined use of Au/TiO_2 microspheres and the packed-bed mode. This is the first demonstration of this kind of design. In this thesis, detailed discussions will be presented to cover the design and analysis of microfluidic reactors, the methodology and the experimental studies.

In the first part, the design of the packed-bed microfluidic reactor are elaborated and then compared with the commonly-used film-mode microfluidic reactor. Theoretical analysis and COMSOL simulation have found that the μPPBR significantly enhances the mass transfer but at the cost of much increased pressure drop.

In the second part, the preparation procedures of Au/TiO_2 microspheres are elaborated, and the fabrication processes of different microfluidic reactors are discussed. These serve as the methodology of this research.

The last part of research presents the experimental results, including the material characteristics and the photodegradation efficiencies. It is found that the Au/TiO_2 microspheres are 2 – 3 times faster than TiO_2 microspheres, and the μPPBR is enhanced by 3 – 4 times as compared to the film-mode reactor. The combined use of Au/TiO_2 in the μPPBR enables an enhancement factor of 8 times as compared to TiO_2 in the film-mode reactor.

In conclusion, this research has presented an original design of microfluidic reactor that seamlessly integrates the LSPR effect and the packed-bed mode of reactor. The new design has experimentally shown an enhancement factor of 8 in the photodegradation efficiency as compared to the TiO_2 film-mode reactor. This reactor can be further improved by optimizing the microsphere size and may be used for other photocatalytic applications such as photosynthesis and water splitting.

List of Publications

Journal papers:

[1] **Pui Hong Yeung**, Yat Lam Wong, Xuming Zhang*, Lab-on microfluidic reactor with different packed modes of plasmonic photocatalyst for efficient photocatalytic water purification. (To be submitted)

[2] Chi Chung Tsoi, Xiaowen Huang, **Pui Hong Yeung**, Ning Wang, Weixing Yu, Polly Leung, Xuming Zhang*, Photocatalytic ozonation for sea water decontamination, Environmental Science & Technology. (To be submitted)

[3] Kwun Hei Willis Ho, AiXue Shang, Tsz Wing Lo, Fenghua Shi, **Pui Hong Yeung**, Yat Sing Yu, Xuming Zhang, Kwok-yin Wong, and Dang Yuan Lei*, Plasmonic Au/TiO2-dumbbell-on-film nanocavities for high-efficiency hot-carrier generation and extraction Advanced Functional Materials.

Conference papers:

[1] **Pui Hong Yeung** and Xuming Zhang*, Photocatalytic water purification by using nanomaterial and solar reactor, the 5th European Conference on Environmental Applications of Advanced Oxidation Processes (EAAOP5), 25th-29th June 2017, Prague, Czech Republic.

[2] **Pui Hong Yeung**, Chi Chung Tsoi, Ning Wang and Xuming Zhang*, Photocatalytic water purification by using nanomaterial and solar reactor, The 7th International Multidisciplinary Conference on Optofluidics (IMCO2017), 25 – 28 July 2017, Singapore, paper sciforum 011422.

[3] Chi Chung Tsoi, **Pui Hong Yeung** and Xuming Zhang*, Solar reactor for photocatalytic water purification, The 7th International Multidisciplinary Conference on Optofluidics (IMCO2017), 25 – 28 July 2017, Singapore, paper sciforum-012821. (Best Poster Award)

Acknowledgements

Here, I would like to express my gratitude to many people who have provided support and assistance during my research.

First, I would like to express my sincerest appreciation to my chief supervisor **Dr. Xuming Zhang** for constant guide for more than two years. His advice and encouragement help in many aspects of my research work. I am also grateful to the collaborator **Prof. Weixing Yu** from Xi'an Institute of Optics & Fine Mechanics, the Chinese Academy of Science for providing the materials in this research. Without their help and support, this research will not be smoothly accomplished.

I would also like to thank my colleague and friends who offer me timely helps and constructive opinions, including Dr. Huan Lin, Dr. Wuxiao Liu, Dr. Xiaowen Huang, Dr. Qingming Chen, Dr. Tenghao Li, Dr. Ning Wang, Dr Yang Liu, Dr Furui Tan, Ms Yujiao Zhu, Mr. Chi Chung Tsoi, Ms. Henrietta Ho, Mr. Yat Lam Wong and Mr. Willis Kwun Hei Ho.

Finally, I would like to express my thank to my family. They encourage me to stand up for every difficulty I have met in these two years. They not only inspire me to be serious in every piece of work, but also instill me with a positive attitude of being a student and a son of my parents.

Table of Contents

List of Figures

List of Tables

Chapter 1 Introduction

1.1 Background

In the last decades, water contamination has been a worldwide environmental problem, especially in developing countries [1]. This worsening issue causes not only an immediate harm to the marine lives, but also poses an irreversible threats to the ecosystem of our Earth [2]. However, water treatment plant usually requires multi-steps to purify the contaminated water for environmentally-friendly purpose, however, it is not efficient. In the research field, semiconductor photocatalyst has been advocated widely because it is normally non-toxic to environment. Photocatalyst, usually made of heterogeneous catalysts [3], has been modified to make water purification feasible under the irradiation of light. This could pave the way to using different photocatalysts to degrade the effluents. Nevertheless, it is still not mature enough for industry scale applications due to the limits of efficiency and cost effectiveness. More work is pending to develop more efficient photocatalyst materials, to understand the mechanisms and to build up new designs of reactors.

Microfluidics is the science of manipulating small amount of liquid sample using the microfabricated channel network with dimensions in the micrometer scale. In the field of environmental engineering, it has shown big potential in sample analysis [4]. This technology has many useful merits, one of which is the use of small amount of sample for detection [5]. Microfluidic reactor made of polydimethylsiloxane (PDMS) can restrain a small volume for fast chemical reaction rate [6]. In addition, PDMS has the characters of flexibility, environmental-friendliness and high transparency [5]. With the aid of the chamber sandwiched by the PDMS and

the glass substrate, a reaction chamber of different patterns can be made to analyze the microfluidic phenomenon.

1.2 Working mechanism of photocatalysis

The photocatalysis usually involves oxidation and reduction reactions during the interaction of the photocatalysts and the organic pollutants. A brief illustration is shown in **Figure 1.1**. Generally, an incoming light photon with the energy $hf \geq E_o$ (band-gap energy) strikes on the surface of the photocatalyst (e.g., TiO_2 and Au/TiO_2), electrons of photocatalysts are excited to the conduction band, leaving holes in the valence band. According to the literature data, the band-gap energy for TiO_2 is 3.2 eV, which suggests that it absorbs only the UV light with the wavelength < 388 nm [7].

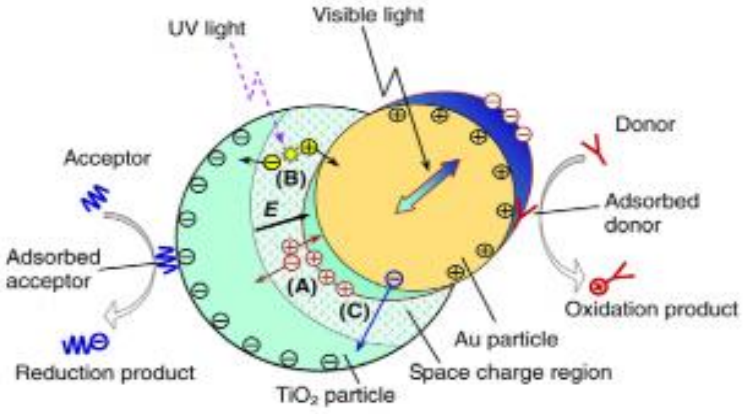

Figure 1.1 The schematic diagram of plasmonic photocatalysis. In general, semi-conductor photocatalyst absorbs photons from light, initializing electron-hole pairs which could help form oxidative radicals for photocatalysis. Au/TiO_2, made of noble metal contacted on TiO_2, could absorb visible light. There are numerous researches on how to boost the efficiency of materials by adjusting the heterojunction band level for suppressing recombination of electrons and holes [8].

The excited electrons and holes would migrate to the surface of semiconductor photocatalyst and then react with the ions in the dissolved water to form reactive species (i.e., radicals) [9]. These are capable of degrading organic pollutants in sewage water. The sequence of the radical reaction in the redox reaction is listed as below [3, 10, 11]:

$$O_2^{\bullet-} + H^+ \rightarrow {}^{\bullet}O_2H \quad \textbf{(1.1)}$$

$$2\,{}^{\bullet}O_2H \rightarrow H_2O_2 + O_2 \quad \textbf{(1.2)}$$

$$H_2O_2 + O_2^{\bullet-} \rightarrow {}^{\bullet}OH + O_2 + OH^- \quad \textbf{(1.3)}$$

$$H_2O_2 \xrightarrow{hf} 2\,{}^{\bullet}OH \quad \textbf{(1.4)}$$

$$H_2O_2 + e^- \rightarrow {}^{\bullet}OH + OH^- \quad \textbf{(1.5)}$$

$$H_2O_2 + h^+ + OH^- \rightarrow H_2O + {}^{\bullet}O_2H \quad \textbf{(1.6)}$$

$$\text{Reactant} + O_2^{\bullet-} \text{ (or } {}^{\bullet}OH) \rightarrow \text{degraded products} \quad \textbf{(1.7)}$$

This is the electron-driven oxidation pathway, in which hydroxyl radicals from **(1.5)** and superoxide radical anions from **(1.1)** are efficient to decompose some organic pollutants such as Methylene Blue (MB) into less harmful products. The color change of dye solution could be observed and linked to the concentration change of the species according to the Beer-Lambert law. The reason for using MB as the indicator solution is that its characteristic absorption peak at 664 nm during degradation does not change, showing that a chain of macromolecule could be broken subsequently by the reactive site of radicals to form less harmful and complex products. Besides, the MB has high molar absorptivity [12] and can be decolorized by photocatalyst under light [13]. This makes it easy to experimentally evaluate the degradation rate.

Titanium dioxide (TiO_2) has recently shown to be effective and low-cost photocatalyst [14], with a high surface-area-to-volume ratio (SA:V). On the other hand, TiO_2 has its own

Achilles heel because it does not absorb visible light, making it not feasible to use the solar light (only 5% energy in UV range) [7]. In addition, its high recombination rate of excited electrons and holes [15] is another pitfall for its overall poor photodegradation performance.

It is strikingly interesting to know that TiO_2 doped with different noble metals (e.g., Au, Ag) could alleviate the problems mentioned above. Localized surface plasmonic resonance (LSPR) in Au/TiO_2 has been shown to significantly enhance the excited electron and hole pairs for photocatalysis [8]. When the incident light with varying electromagnetic field strikes on the Au nanoparticles, it drives the collective oscillation of free electrons that is in phase with the incoming light wave [8]. Besides, the LSPR can provide an intensive local electric field depending on the size and geometry of the Au nanoparticles, this can be used to tailor-make the plasmonic effect for photocatalysis.

Normally, photocatalysts may contain excess electrons and oxygen defects. TiO_2 is an n-type material which has a Fermi level close to the conduction band [16]. In this research, a structure in physical contact with Au nanoparticles is generated. After fabrication, Au nanoparticles could absorb visible light while TiO_2 absorbs UV light. As a result, Au/TiO_2 absorbs both visible light and UV light. Owing to the phenomenon of LSPR, collective oscillation of electrons, known as plasmons, can excite more electrons and holes for TiO_2. After the equilibration of Fermi levels of two different materials, it provides a fast lane for some plasmon-excited hot electrons to move to the conduction band of TiO_2 [8, 17]. Here TiO_2 and Au could perform its photodegradation function simultaneously.

It is noted that the fast recombination rate of electrons and holes causes a dramatic reduction of the photodegradation efficiency. A space-charge region near the surface of Au could

prevent the excessive carriers to combine with their counterparts. Such junction enhances the separation of the photo-excited electrons and holes, thus suppressing their direct recombination [18].

The performance of photocatalysis could be tested using a microfluidic reactor. When light initiates the photocatalyst to degrade the dye indicator, the collected sample can be analyzed by measuring the absorption spectrum. After the photocatalytic reactions, photocatalyst would decompose a wide range of organic pollutants into less harmful species (e.g., CO_2, H_2O).

1.3 Objectives

In this report, different designs of microfluidic reactors will be examined to explore the optimum photocatalytic efficiency for decontaminating organic pollutants. Furthermore, we will experimentally present how microfluidic reactors could enhance the photodegradation effect by using the plasmonic photocatalysts. More specifically, this research will focus on the following three major parts:

(1) Analysis of different packing modes of plasmonic photocatalysts in the microfluidic reactor. In this research, two kinds of packing are tested, namely, film mode and stuffed mode. These could realize the merit of high SA:V of particles inside the chamber for photodegradation.

(2) Experimental comparison of the performances of TiO_2 and Au/TiO_2. Both pure TiO_2 and Au/TiO_2 are immobilized into the microfluidic reactors. This is to verify that the LSPR could indeed enhance the photodegradation in visible light.

(3) Simulation of the fluidic dynamics inside the microfluidic reactor. Some parameters will be studied, such as pressure drop along the chamber, velocity distribution and Reynolds

number, etc. These are major fluidic parameters for the estimation of the internal environment.

1.4 Outline of the thesis

Chapter 1 introduces the background of microfluidics for water purification and the working mechanism of the photocatalysis. Objectives of the research are also included to show the scope of research.

Chapter 2 is the literature review, which describes the reported microfluidic reactors which are different from my design. For comparison, all microfluidic reactors will be discussed thoughtfully in terms of working principles and applications. Some merits and drawbacks should be included in this section.

Chapter 3 highlights my own design of microfluidic reactor. Some parameters concerning microfluidic reactors are discussed and analyzed by simulations.

Chapter 4 summarizes all fabrication and experimental procedures. These are important operations before data collection.

Chapter 5 presents all experimental results, including the material and device characterization, and the photodegradation results of film-mode and stuffed-mode microfluidic reactors. Comparisons are conducted to show which one has better photodegradation efficiency.

Chapter 6 concludes the thesis with major achievements and findings. Future work on improvement of the whole design will be also presented to further increase the robustness of device for more practical applications.

Chapter 2 Literature Review

In this chapter, the evolution and development of reactors will be reviewed. First, the reactor designs will be categorized to find out which one is more suitable for photocatalytic microfluidic reactor. Different geometric designs possess different specific utilities, some will be presented. The last part is a discussion on the arrangement of particles inside the microfluidic reactor.

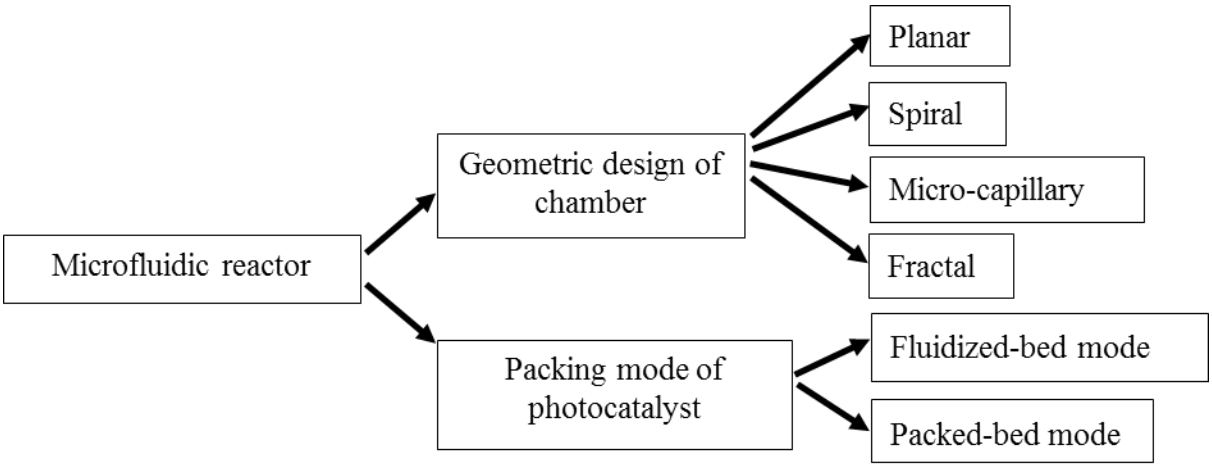

Figure 2.1 Categories of microfluidic reactors

2.1 Geometric design of reactor

Most of the reported microfluidic reactors can be categorized by the geometric design of chamber or the packing mode of photocatalyst, as shown in **Figure 2.1**. Microfluidic reactor is the compact device for a variety of reactions. For different purposes ranging from simple analysis of chemical species to continuous tracing of solutions in the integrated network of microfluidics, the device would be designed with different geometries and different shapes.

The design of the microfluidic reactor would vary significantly, therefore, it is important to generalize the typical designs of the device and to examine their characteristics. This would help us understand the trend of microfluidics and try to exploit their merits for our device. As shown in **Table 2.1**, there are four typical designs: planar, spiral, micro-capillary and fractal, named after the reactor shapes.

Table 2.1 List of reactor geometries

	Planar	**Spiral**	**Micro-capillary**	**Fractal**
Advantages	• High capacity • Uniform reaction rate	• Low fluidic resistance • Negligible hindrance	• Steady fluidic flow	• Non-linearity kinetics
Disadvantages	• Relative long diffusion length	• Low capacity	• Hard to control thickness	• Complicated design

2.1.1 Planar microfluidic reactor

This design is the simplest, most-adopted one for the microfluidic reactor. Literally, planar microfluidic reactor consists of a planar central chamber for chemical reaction. It is similar to my own microfluidic reactor, which is also user-friendly and easy for fabrication. Because of this high symmetry and relative high capacity, it is usually suitable for studying the efficiency of the chemical reaction, such as photocatalysis. An example of planar microfluidic reactor is shown in **Figure 2.2**.

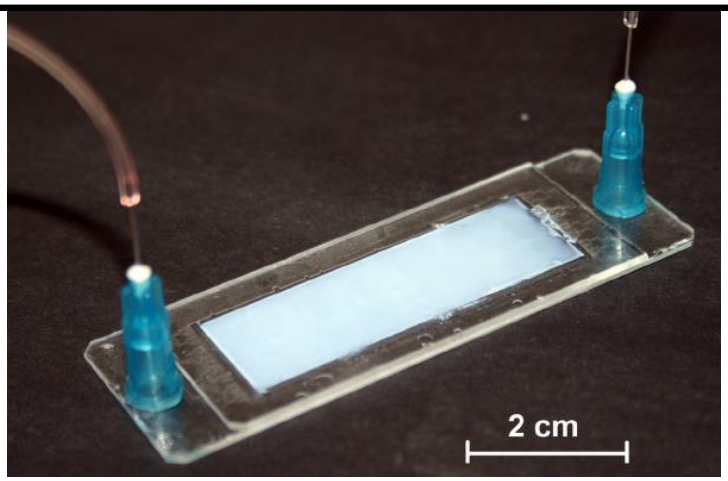

Figure 2.2 The planar reactor contains white TiO_2 film on the substrate and is encapsulated by the glass slides to make a sealed central chamber. Two ends are made as the inlet and outlet for guiding fluid flow in microfluidic device [19].

Advantages of planar microfluidic reactor:

1) Manipulation of a relatively huge amount of sample. It allows to investigate the chemical reaction by several methods, such as finding reaction rate by colorimetry, and by the measurement of absorption spectrum.

2) Uniform reaction rate. In the planar microfluidic reactor, fluid is usually driven by the capillary channel before entering the central planar chamber. This is especially important if the quality of adsorption and desorption in photocatalysis should be ensured. It is also easy to immobilize particles inside this device due to its large volume.

2.1.2 Spiral microfluidic reactor

Another meaningful design called spiral microfluidic reactor is usually made for microfluidic water purification. As shown in **Figure 2.3**, the round-shaped channel is usually beneficial for fluid to follow without too much fluidic resistance relative to the channel wall. The restriction of small amount of fluid along the pathway of the spiral enables the long reaction pathway for reaction, facilitating more dedicated microfluidic system.

Figure 2.3 Spiral channel is a prevalent pattern for guiding fluid to the reaction chamber because of insignificant fluid flow resistance in the channel.

Advantages of spiral microfluidic reactor:

1) Relatively low fluidic flow resistance. Since the channel of the spiral contains smooth turnings, it allows fluid to flow in a steady way. If the flow pattern varies along the flow pathway, it would affect the accuracy of result.

2) The versatility of the pattern. This pattern may be developed to have a multi-deck of the spiral in the microfluidic reactor, when the light normally irradiates on the multi-deck, light shining on the fluid of each deck would not be hindered. A simplified diagram is shown in **Figure 2.4**.

Besides, this pattern would allow more fluids from individual spiral line to mix with each other at the connection point by inserting more inlets that are connected to the spirals.

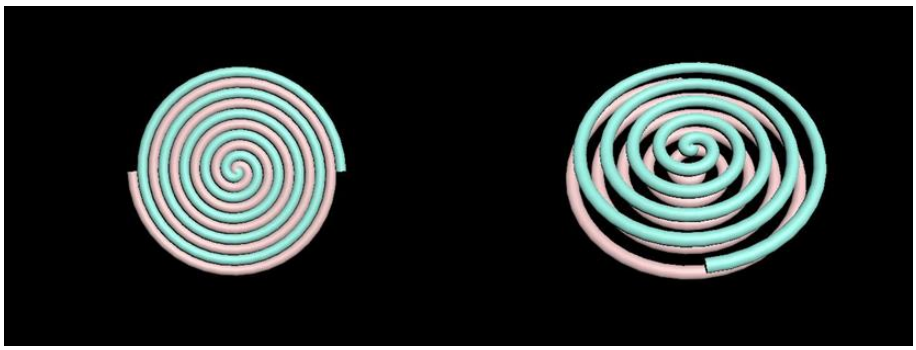

Figure 2.4 The top view of double-deck spiral channel is shown on the left, which shows a more complex microfluidic design. If light irradiates in the direction normal to the plane, every section of the path will receive light without hindrance. Often, the whole design could be made in multi-decks.

2.1.3 Micro-capillary reactor

Next interesting device is made of micro-sized capillary tubes containing photocatalyst. As shown in **Figure 2.5**, this structure could increase the contact area of MB and photocatalyst because MB would flow smoothly inside the channel and would be adhered to the inner surface of the capillary tube full of uniformly packed photocatalyst particles. Moreover, this method is easy to control by adjusting the flowing rate of MB for long residence time of dye inside the chamber.

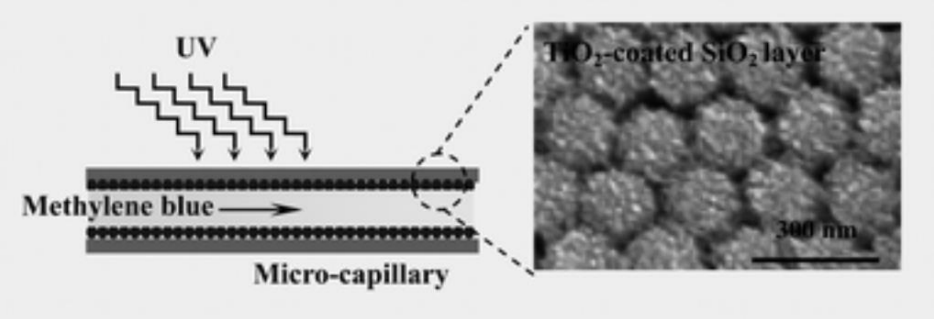

Figure 2.5 The cross-section view of micro-capillary microfluidic reactor shows typical packing mode of photocatalysts, which facilitates the continuous flow of MB and interaction chance [20].

Advantages of micro-capillary reactor:

1) Steady fluid dynamics. Since most photocatalysts are attached to the inner surface of the capillary tube, the flow of MB would be hindered insignificantly. Since the flow of fluid is relatively constant along the path, the experiment result would be more accurate with constant reaction time.

Disadvantages of Micro-capillary microfluidic reactor:

1) The coating of photocatalyst particles on the inner surface is troublesome and difficult to control. Non-uniformity of particles on the inner surface would make this device less functional because it may cause the reaction rate to vary along the path. Another major drawback is that the upper layer obstructs the light from reaching the lower layer. The thickness and uniformity of photocatalyst should be considered simultaneously.

2.1.4 Fractal microfluidic reactor

Fractal microfluidic reactor is a device for complex analysis of the small number of samples, it is usually exploited in biomedical engineering. As shown in **Figure 2.6**, fractal design means a geometric pattern that repeats itself under some level of magnification. Therefore, the fractal pattern should be tailor-made for appropriate flow regime in different sections. Another trait is that it is usually composed of highly symmetric ring pattern, which allows thorough mixing and transfer of fluid [21]. A fractal pattern could be realized by using the following picture.

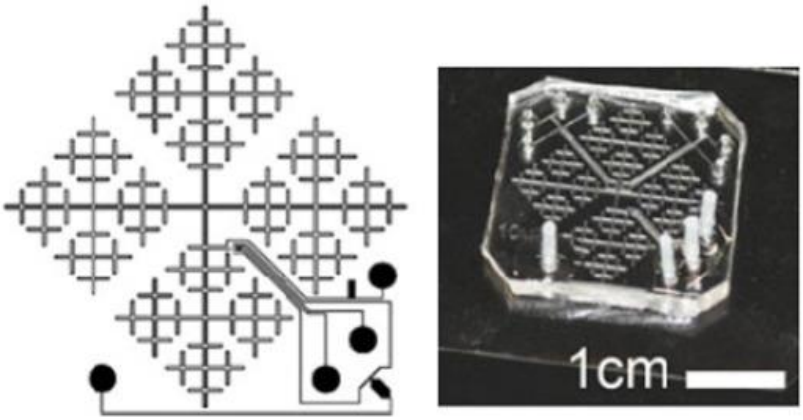

Figure 2.6 Fractal microfluidic reactor enables more complex design of pattern and different reaction centers for analyzing non-linear kinetics of sample [22].

Advantages of Fractal microfluidic reactor:

1) Non-linearity kinetics. The fractal shape could enable a nonlinear reaction courses that vary with time scales. The relationship could be changed by power relationship. By detecting the fluorescence of multiple points in the channel, the reaction kinetics in several time scales can be acquired by integrating the channel at every given distance into fractal shape.

2.2 Different packing modes of the photocatalyst

In the previous sub-section, it combines the geometries of microfluidic reactor with their respective characteristics. However, the packing arrangement of particles in the microfluidic reactor is also important. The arrangement of photocatalyst particles inside are of interest to enhance overall efficiency of chemical reactions. Popular ones like the fluidized-bed mode and the packed-bed mode, shown in **Table 2.2**, have been widely used to boost the efficiency of the chemical reaction.

Table 2.2 List of packing arrangements of photocatalysts

	Fluidized-bed	**Packed-bed**
Advantages	i. High intermixing of particles	i. Higher conversion per weight
Disadvantages	i. Suitable Temperature required ii. High pumping velocity iii. Hard to recycle particles	i. High pressure drop

2.2.1 Fluidized-bed reactor (FBR)

Fluidized bed reactor is a mixture of solid and fluid, which could be collectively treated as fluid in the reactor. In **Figure 2.7**, the fluid is passing through the reactor filled with granular catalyst particles, thereby suspending particles like a fluidized bed. This technology is widely utilized in traditional power industry.

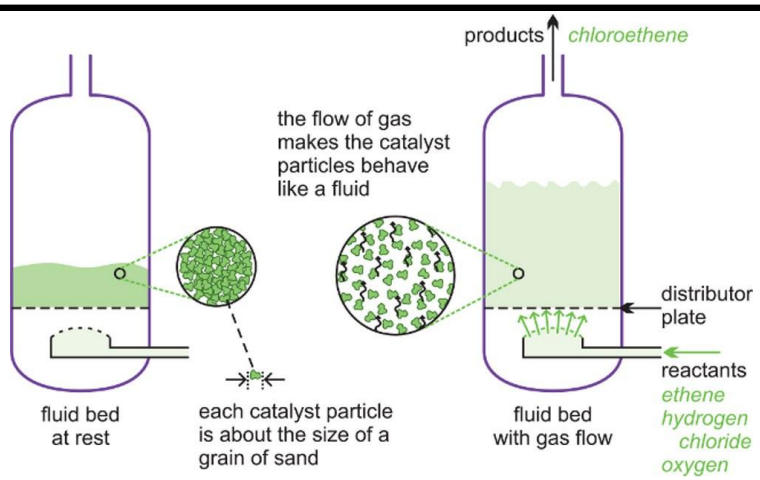

Figure 2.7 The above schematic illustrates reactants are pumped into the fluid bed with high velocity, the reactant mixture behaves like a flowing fluid in the reaction chamber. Reference: http://www.essentialchemicalindustry.org/processes/chemical-reactors.html

The typical industrial reactor is exemplified in **Figure 2.7**. First, the still bed which is made of many catalyst particles is injected with the fluid, such as gas or liquid. The fluid composed of all constituents will move together through the reactor. This operation needs to be driven by injecting pressure and velocity. Sometimes, a suitable temperature is also necessary.

The FBR has many merits over the packed-bed reactor, such as large contact area and high chance between the solid particles and the fluid. First, the FBR enhances the intermixing of particles and the interaction area in reaction mixture. It enables nearly a uniform temperature in the reactor, and enhances reaction rate readily than other methods[23]. Besides, the FBR usually handles small particles, thus avoiding clogging and high pressure drop.

However, this technique cannot be applied to all applications because the fluidized bed is not immobilized and is moved by the incoming fluid. The diagram shown in **Figure 2.8** reveals that the velocity of the mixture is relatively high, which is not favorable for the microfluidic reactor.

There is a minimum fluidization velocity [24] to maintain a constant pressure drop along the chamber. It is necessary to adjust the fluid velocity to make constantly fluidized particles before the experiments are conducted. However, fast movement of particles tends to break the microfluidic device.

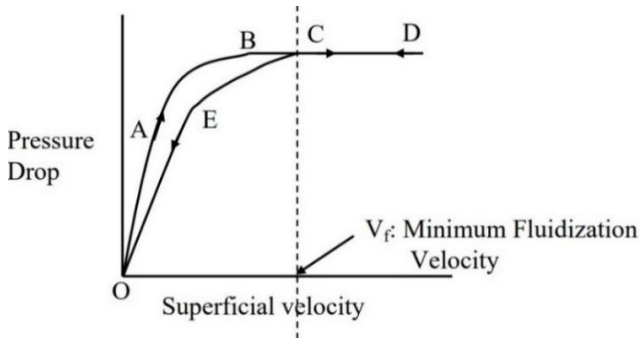

Figure 2.8 Relationship between the pressure drop and the superficial velocity. Normally, there is a minimum fluidization velocity to maintain the pressure drop between two ends. The ABCD path means the pressure drop with the increasing superficial velocity, while the DCE path means the pressure drop with the decreasing fluid velocity. E is lower because the fluid has been restored to loosely packed state at low velocity [23].

Besides, it is hard to recycle the photocatalysts after photocatalysis [25]. For the FBR, the mixture of liquid and solute would disperse uniformly in the chamber, making it tedious to recycle the used photocatalysts. This is unfavorable in the experimental scale and even in the industry since photocatalysts needs to be removed in the reactor.

2.2.2 Packed-bed reactor (PBR)

Packed-bed reactor (PBR) is an alternative to the FBR. In principle, catalyst particles are usually filled and immobilized inside the chamber as illustrated in **Figure 2.9** [26]. Sometimes, it is also

called fixed-bed reactor or stuffed-mode reactor. This mode has been widely utilized in chemical industries, such as wastewater engineering.

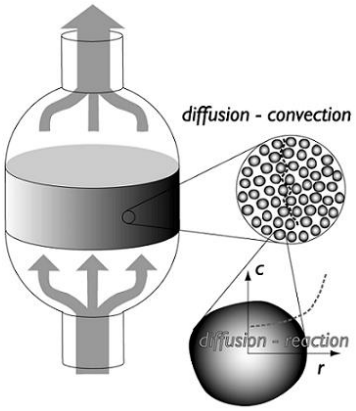

Figure 2.9 Industrial packed bed reactor in which the flow comes from macro-size (bed porosity) and micro-size (particle porosity) if the particles are mesoporous. https://www.comsol.com/blogs/packed-bed-reactor/

The chemical reaction usually takes place on the surface of the catalysts. This grants the PBR a special advantage, higher conversion per weight of catalyst than other catalytic reactors. In this reactor, the amount and the packed arrangement of particles play a more important role in optimizing the efficiency of the chemical reaction.

However, one of the major disadvantages is the changing flow characteristic because of the alteration in the bed porosity in the chamber. Therefore, the pressure drop and the bed compaction must occur, they should be considered in the design of the reactor. Usually in industry, the reactor and the sample utilizing the packed bed catalysts could be enlarged to a large scale to handle a massive amount of effluent every day.

In the PBR, numerous catalyst particles with different shapes have been tested, as tabulated in Table 2.1. It is noted that D/d_s (where D is the length of the bed, d_s is the equivalent volume sphere diameter $[(6Vp/\pi)^{1/3}]$) is an important parameter for analyzing the influence of the wall upon the fluid flow. If D/d_s is smaller than 40, the wall effect to the flow is negligible. Otherwise, the friction effect from the wall certainly imparts the overall pressure drop. There are some parameters listed in **Table 2.3** that influence the fluid flow in the channel. As the photocatalysts used is spherical, it would be highlighted more.

Table 2.3 Influence of the particle shape on the fluid dynamics in the packed-bed reactors [27].

Shape	**φ_s***	**$d_p \times h_p \times d_i$ (mm)**	**d_s (mm)**	**d_e (mm)**	**D/d_s**	**Materials**	**ε****
Spheres	1	1.66	1.66	1.66	24.7	γ-Al_2O_3	0.382-0.431
Spheres	1	2.10	2.10	2.10	19.5	Glass	0.385-0.431
Spheres	1	2.57	2.57	2.57	16.0	γ-Al_2O_3	0.396-0.429
Spheres	1	3.50	3.50	3.50	11.7	γ-Al_2O_3	0.400-0.443
Cylinders	0.866	3.2 × 4.2	4.03	3.49	10.2	γ-Al_2O_3	0.368-0.420
Cylinders	0.782	1.6 × 4.7	2.62	2.05	15.7	γ-Al_2O_3	0.437
Cylinders	0.672	1.3 × 7.5	2.67	1.80	15.4	γ-Al_2O_3	0.484-0.526
Rings	0.590	3.2 × 5 ×1.3	4.25	2.35	9.7	γ-Al_2O_3	0.474
Trilobes	0.630	1.27 × 5.5	2.54	1.41	16.1	Ni-Mo	0.466-0.511
Quadralobes	0.593	1.35 × 5.2	2.13	1.26	19.3	Ni-Mo	0.471-0.502

φ_s* (dimensionless): sphericity of particle;

ε** (dimensionless): bed porosity.

Besides, the porosity of the packed bed is not fully realized, which makes the pressure drop by the empirical equation.

$$\frac{\Delta P/L}{\rho_\alpha g} = A\frac{Re_\alpha}{Ga_\alpha} + B\frac{Re_\alpha{}^2}{Ga_\alpha} \quad \textbf{(2.1)}$$

where A (=150) and B (=1.75) are known as the Ergun constants, G_α is the dimensional Galileo number of the phase. These constants are affected by the bed porosity, which changes the value of pressure difference. Experimental-determined Ergun constant may be collected or evaluated accurately by doing numerous experiments beforehand. It is also found that spherical particles in the reactor well agree with **Equation (2.1).**

It is seemingly doubtful that the PBR adds more uncertainties in determining the pressure difference experimentally. However, thanks to the aid of software, the fluid flow can be demonstrated in the microfluidic reactor graphically, this would open more room for adjusting the dimension of parameters before making the microfluidic reactor with optimum efficiency. If the microfluidic PBR is developed for quick analysis of material performance in photocatalysis, it would be very useful in different fields, such as chemical engineering.

2.3 Summary

This chapter has categorized the major designs of reactors in the aspects of the geometries and the packing modes of particles. Two criteria are used to evaluate which design of reactors is selected for fabrication. First, when it comes to the reactor shapes, it is important to realize what reaction kinetics and mechanism to explore. As the major purpose of the experiment is to determine the photocatalytic efficiencies of different photocatalytic materials, the planar reactor design may be

a suitable one. It uses a central chamber to hold the photocatalysts. Besides, the packed mode is worth discussing since it could examine the effect of surface-area-to-volume ratio of particles inside the microfluidic reactor. In the next chapter, a microfluidic reactor with the specific design will be presented and analysis will be conducted to process the preliminary results of the designed microfluidic reactor.

Chapter 3 Design & Analysis

The research insight of different reactors inspires the idea to apply photocatalysis into microfluidics. It is one of the applicable goals in this research if a portable and user-friendly device is utilized for the photocatalytic water purification. Based on the previous literature review, two modes of microfluidic reactors are here developed to enhance the reaction rate and the efficiency of photodegradation of organic pollutants. More specifically, a film-mode microfluidic reactor and a stuffed-mode microfluidic reactor are developed to investigate their respective characteristics. These initiate the intensive research on how the microfluidic reactor could be functionalized for photocatalysis. Fluid stability and LSPR in the microfluidic reactors are simulated by COMSOL and FDTD, respectively.

3.1 Film-mode microfluidic reactor

A thin layer of the photocatalyst is deposited on the top of the glass substrate of the microfluidic reactor. It is not necessary to filter the degrading sample since the photocatalyst film is attached firmly on the glass slide [28]. As shown in **Figure 3.1(a)-(c)**, very small amount of the photocatalyst material is required for the film-mode microfluidic reactor as the film is still thin (~2-4 μm) compared with the height of the chamber (~40 μm).

3.2 Stuffed-mode microfluidic reactor

Stuffed-mode microfluidic reactor is new design and different from the conventional designs. The photocatalyst particles are injected and thus immobilized inside the chamber, making the distance between particles throughout the chamber very small. This ensures that the stuffed-mode

microfluidic reactor has large surface area of photocatalysts for photodegradation of MB [29]. The fabricated stuffed-mode microfluidic reactor is shown in **Figure 3.1(d)-(f)**.

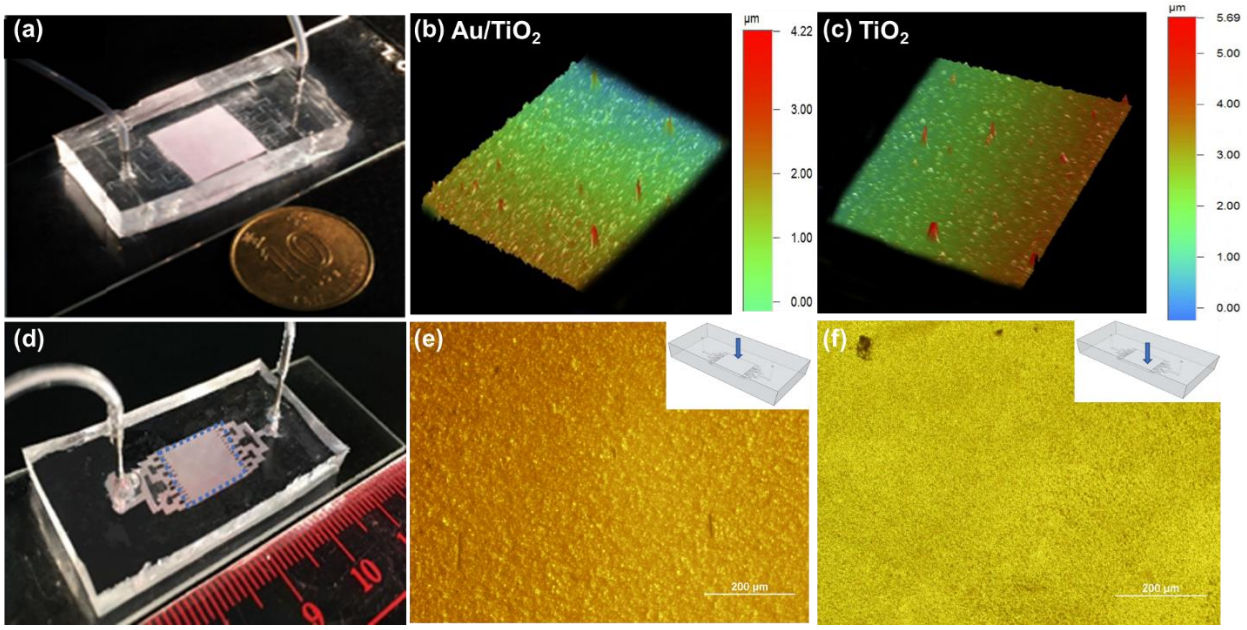

Figure 3.1 (a) The film-mode microfluidic reactor was fabricated by rolling a 1cm x 1cm photocatalyst film on the glass substrate, the colour part represents the central reaction chamber. (b) The morphology of Au/TiO_2 film as measured by DektakXT Surface Profiler, the thickness was uniform and 1 to 2 μm. (c) The morphology of TiO_2 film, which was deposited on the glass substrate to form a film-mode microfluidic reactor. (d) The stuffed-mode microfluidic reactor filled with Au/TiO_2. The blue dotted line represents the central chamber of microfluidic reactor. (e) The photocatalysts were injected into the stuffed-mode microfluidic reactor before solvent is dried out. (f) The dried photocatalysts in the stuffed-mode microfluidic reactor

During fabrication process of microfluidic reactor, some important parameters such as the dimensions of reactors and particles size were measured. The comparison of two modes microfluidic reactor is listed in the **Table 3.1** as shown below:

Table 3.1 The table listing the major structural parameters of two mode microfluidic reactor.

	Film-mode	**Stuffed-mode**
Micro-chamber (Length × Width × Height) (μm)	10000×10000×40	10000×10000×40
Film thickness (μm)	1 to 2	Null
Particles shape / radius (μm)	Sphere TiO_2 (300 to 400 nm)	Sphere Au/TiO_2 (300 to 400 nm)

3.3 Comparison of different modes of microfluidic reactors

Two modes of microfluidic reactors have distinct features, which could be deduced by some parameters, such as the surface-area-to-volume ratio and the fluid properties like the Reynolds number. Since two modes have different structures, the theoretical and simulation results are useful to make a comparison.

3.3.1 Analysis of surface-area-to-volume ratios of two modes

The film mode and the stuffed mode of photocatalyst are with two distinct packing of particles inside the sensitive microfluidic reactor. The major difference comes from their respective surface-area-to-volume ratio (SA:V) of the particles inside the chamber. Using the parameters in **Figure 3.2**, one can get:

$$\text{(Film mode)}\ \frac{SA}{V}=\frac{A}{V}=\frac{WL}{WLh}=\frac{1}{h} \tag{3.1}$$

$$\text{(Stuffed mode)}\ N=\frac{H}{D}, K=\frac{W}{D}, M=\frac{L}{D} \tag{3.2a}$$

$$A = \pi D^2 \times \frac{HLW}{D^3} = \frac{\pi HLW}{D} \quad \textbf{(3.2b)}$$

$$\frac{SA}{V} = \frac{A}{V} = \frac{\pi HLW}{HLWD} = \frac{\pi}{D} \quad \textbf{(3.2c)}$$

Therefore, the efficiency factor $\eta = \frac{SSA}{V} = \frac{\pi h}{D} = \frac{\pi(2\times10^{-6})}{450\times10^{-9}} = 13.9$ **(3.3)**

where *W*, *L* and *H* are the width, the length and the height of the chamber respectively; *h* is the height of the film mode; and *D* is the diameter of nanoparticles.

Since the stuffed-mode microfluidic reactor has a higher SA:V ratio than that the film-mode microfluidic reactor, it allows more adsorption sites and reactive sites for photocatalysis. The stuffed-mode microfluidic reactor is thus worth investigation to see whether the experimental result is consistent with this analysis. It also arouses the interest to study how to utilize such many random particles for the microfluidic reactor.

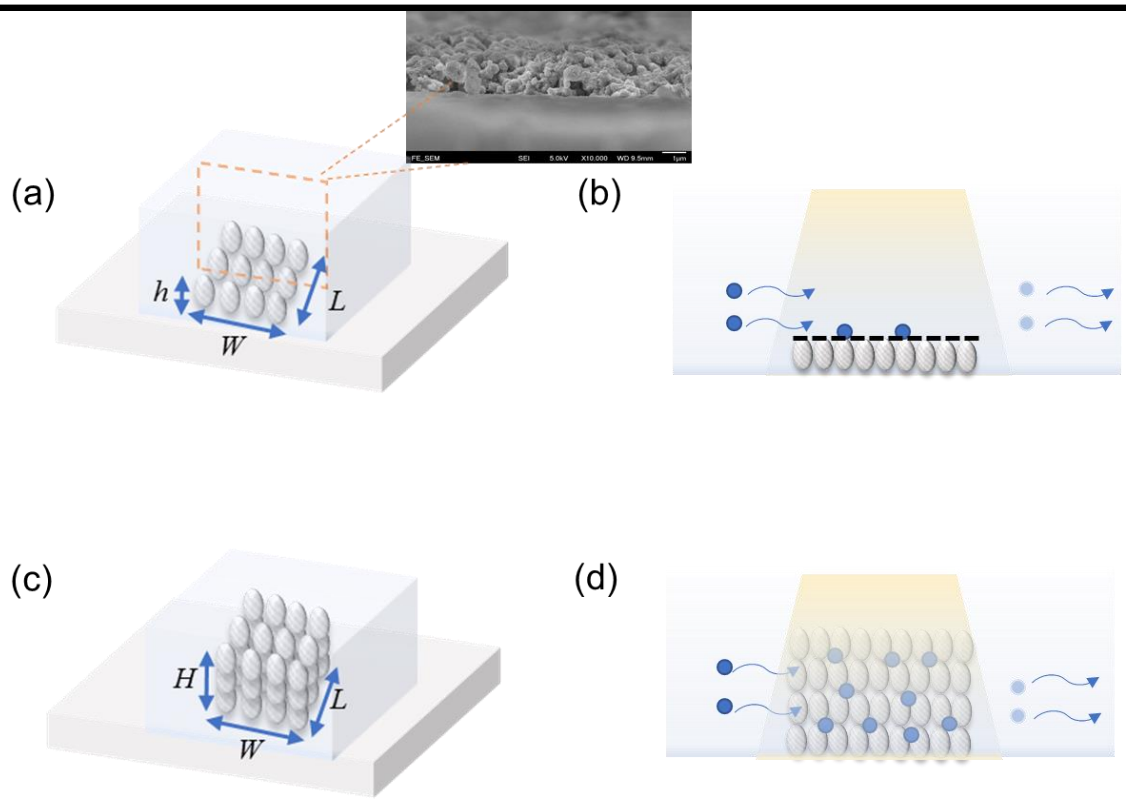

Figure 3.2 (a) The film-mode microfluidic reactor has a film of photocatalyst on the glass substrate. The inset shows the SEM graph of film, indicating the thickness and morphology of photocatalyst. (b) The cross-section view illustrates that the major absorption area is on the top of the thin layer. (c) The stuffed-mode microfluidic reactor assumes the particles are packed inside the chamber. (d) Every surface of particles could absorb MB, resulting in a high SA:V ratio of this device.

3.3.2 Analysis of fluidic performance

Ideally, the stuffed-mode microfluidic reactor only provides more photocatalyst particles for dye molecules to adhere to. However, the dye fluid should be considered carefully as well. If the fluid could not flow steadily in the microfluidic reactor, the usefulness of the microfluidic reactor for photocatalysis would fall into the shadow. In this aspect, two parameters are specifically examined,

namely the Reynolds number and the pressure changes. The former indicates whether it is laminar or turbulent, while the latter one is associated with the energy efficiency of pumping source. A large pressure drop simply means it consumes more pumping power to have a constant velocity of fluid inside.

3.3.2.1 Film-mode microfluidic reactor

In the film-mode microfluidic reactor, a thin layer of photocatalyst is deposited on the substrate of the chamber as shown in **Figure 3.2(b)**. The fluid could flow easily except at the boundaries, due to the wall and the film roughness. Moreover, one important parameter for the flow property of fluid is Reynolds number (Re), which is defined as the ratio of the inertia force to the viscous force.

The aspect ratio α^* for a rectangular channel of width *w*, and height *b* is given by [30, 31]:

$$\alpha^* = \frac{b}{w} = \frac{3.8\times10^{-5}}{0.01} = 3.8\times10^{-3} \leq 1$$

$$Re = \frac{\rho V_S D_h}{\mu} \quad \textbf{(3.4)}$$

$$Re = \frac{1000\times2.19\times10^{-3}\times7.57\times10^{-5}}{1.03\times10^{-3}} = 0.161 \quad \textbf{(3.4a)}$$

The Re value for the film-mode microfluidic reactor is much smaller than 1 at four different flow rates. Therefore, the fluid behaves like a laminar flow inside the microfluidic reactor.

$$f = \frac{C}{Re} \quad \textbf{(3.5)}$$

$$C = 24(1-\alpha^*-1.3553\alpha^*+1.9467\alpha^{*2}-1.7012\alpha^{*3}+0.9564\alpha^{*4}-0.2537\alpha^{*5}) \quad \textbf{(3.5a)}$$

$$f = \frac{C}{Re} = \frac{23.786}{0.161} = 147.7 \quad \textbf{(3.5b)}$$

where *C* is the coefficient that represents the new friction factor depending on the geometries of the cross-section of the channel [30, 31].

$$\Delta P = \frac{4 f L \rho V_S^{\,2}}{2 D_h} \quad \textbf{(3.6)}$$

$$\Delta P = \frac{4 \times 147.7 \times 0.01 \times 1000 \times (2.19 \times 10^{-3})^2}{2 \times 7.57 \times 10^{-5}} = 187 \text{ Pa} = 0.00185 \text{ atm} \quad \textbf{(3.6a)}$$

D_h: Hydraulic diameter of rectangular cross-section channel = $\frac{4 \times \text{Area}}{\text{Perimeter}}$ = 7.57×10^{-5} m,

f: Fanning friction factor,

ρ: Density of the fluid= 1000 (kg/m^3),

μ: Dynamic viscosity of the fluid=1.03×10^{-3} (Pa·s),

Vs: Superficial velocity=2.19×10^{-3} (m/s) for 50μl/min ($V_s = \frac{Q}{A}$, where *Q* is the volumetric flow rate of the fluid and *A* is the cross-sectional area of the bed),

ε: Void fraction of the bed (the ratio of the void volume to the total volume of the bed) = 0.48

3.3.2.2 Stuffed-mode microfluidic reactor

The stuffed-mode microfluidic reactor is assumed to be a packed bed reactor in which many tiny particles are packed inside with pores, as is illustrated in **Figure 3.2(c)**.

The fluid also behaves like a laminar flow inside the microfluidic reactor. Besides, to find out the pressure drop in the stuffed-mode microfluidic reactor mathematically, Darcy Law is

applied if the stuffed particles are regarded as a series of parallel bundles packed as a simple cubic structure [32]. The experimental Reynolds number and its pressure change along the chamber are listed as follows [33],

$$Re_p = \frac{U D_p \rho}{\mu(1-\varepsilon)} \tag{3.7}$$

$$Re_p = \frac{0.00208 \times 450 \times 10^{-9} \times 1000}{1.03 \times 10^{-3} \times (1-0.3)} = 0.00130 \tag{3.7a}$$

$$\Delta P = 72 \frac{U \mu L (1-\varepsilon)^2}{D_p{}^2 \varepsilon^3} \tag{3.8}$$

$$\Delta P = 72 \frac{2.083 \times 10^{-3} \times 1.03 \times 10^{-3} \times 0.01(1-0.3)^2}{\left(450 \times 10^{-9}\right)^2 0.3^3} = 138\,\mathrm{MPa} = 1366\,\mathrm{atm} \tag{3.8a}$$

Re_p: Reynolds number for the packed bed

U: Superficial velocity for packed bed (m/s), taking the pumping rate to be 50 μl/min.

D_P: Particle diameter (m)

ρ: Fluid density (kg/m^3),

μ: Dynamic viscosity (Pa·s),

ε: Porosity fraction.

From **Equation (3.8a)**, although the pressure drop of the stuffed-mode microfluidic reactor is large, it could be minimized if the bed length is shortened or the diameter of photocatalyst

particle is increased. However, it still possesses a high SA:V, which results in a high mass transfer rate for reactions species [34].

3.4 Simulation result of fluidic mechanics

This part supplements the previous numerical result, which adds more information about the flow regime inside the microfluidic reactor, such as the pressure drop along the chamber, the velocity profile and the concentration profile. These parameters could be simulated.

As mentioned in the packed-bed reactor in **Subsection 2.2.2**, the bed with porous packed catalysts makes the modeling of mass transport a challenge because the mass transport could occur in the macro-pores between the dumped pellets and in the micro-pores inside the catalyst pellet. It contains more dimensions for modeling the stuffed-mode microfluidic reactor, therefore, Comsol 5.3 with the module A Multiscale 3D Packed Bed was exploited to handle this multiscale problem in the microfluidic reactor.

In this model, Comsol reacting flow in porous media is used. The reaction conditions are isothermal at temperature 300 K. This is the initial assumption since viscosity, diffusivity and density are a function of temperature. Thus, they are treated as constants in this model.

3.4.1 Mathematical analysis

Navier-Stokes equations are often used to describe the flow of fluid in a porous medium since the stuffed-mode microfluidic reactor leaves random porosity among particles. Assume there are only MB in the reaction chamber.

$$A \rightarrow B$$

where A is the initial MB and B is the photodegradation product.

First, Navier-Stokes equations describe the motion of viscous fluid by considering Newton's second law [35].

Navier-Stokes formula: $F_{inertial} = F_{pressure} + F_{gravity} + F_{viscosity}$

$$m\frac{dv}{dt} = -\int pdA - mg + F_{viscosity}$$

$$\int_V \rho \frac{dv}{dt} dV = -\int_v \nabla p dV - \int_v \rho g dV - \int_v \frac{\mu u}{K} dV$$

When the left part is set to be zero for incompressible flow and negligible acceleration due to the small gravity, the equation would be changed to Darcy law if the medium is porous. Some parameters were added for generalizing the porous medium properties [36].

$$\text{Darcy Law}: Q = -\frac{KA(P_2 - P_1)}{\mu L} \text{ or } q = -\frac{K}{\mu}\nabla p \qquad \textbf{(3.9)}$$

where Q is the discharge rate (units of volume per time, m^3/s),

q is the discharge per area (m/s),

K is an intrinsic permeability of the medium (m^2),

A is cross-sectional area A (units of area, m^2),

$P_2 - P_1$ is a pressure difference of two ends (Pa),

μ is dynamic viscosity (Pa·s)

L is the length over which the pressure drop (m).

3.4.2 COMSOL simulation

Many pores model are based on the capillary tube bundle model. Moreover, the fluid is incompressible and laminar. Default Darcy law was applied to the model which is composed of the square chamber with periodic open channels for entering in and draining out. The pressure goes down significantly inside the reaction chamber as indicated in the previous formula. It is inevitable that the pressure drop is large in a small chamber filled with tiny photocatalysts. Sometimes, the pressure drop is used to determine the pumping power requirement. In addition, it appears that velocity of the fluid in the chamber appears uniformly constant, it is workable if the device is left to be pumped for a while, the pumping-in rate could be nearly same as the pumping-out rate.

The simulated results of the pressure profile and the velocity profile are presented in **Figure 3.3-3.6**. Here the coordinate system XYZ is defined as the X direction for the flow moving, the Y direction for the width of the chamber and the Z direction for the height of the chamber. From **Figure 3.3**, the pressure is uniform in the cross section of any specific location along the X direction (i.e., the flow moving direction); and it drops gradually along the X direction. **Figure 3.4** shows the pressure surface distribution the microfluidic reactor. The pressure drops almost linearly

along the X direction, as can be seen from **Figure 3.3(b)**. Based on the velocity profile in **Figure 3.5**, the velocity is high in the middle region and becomes zero near the boundaries, showing no slipping effect. In addition, from **Figure 3.6**, it indicates that the major velocity component of fluid is in x-direction.

(a)

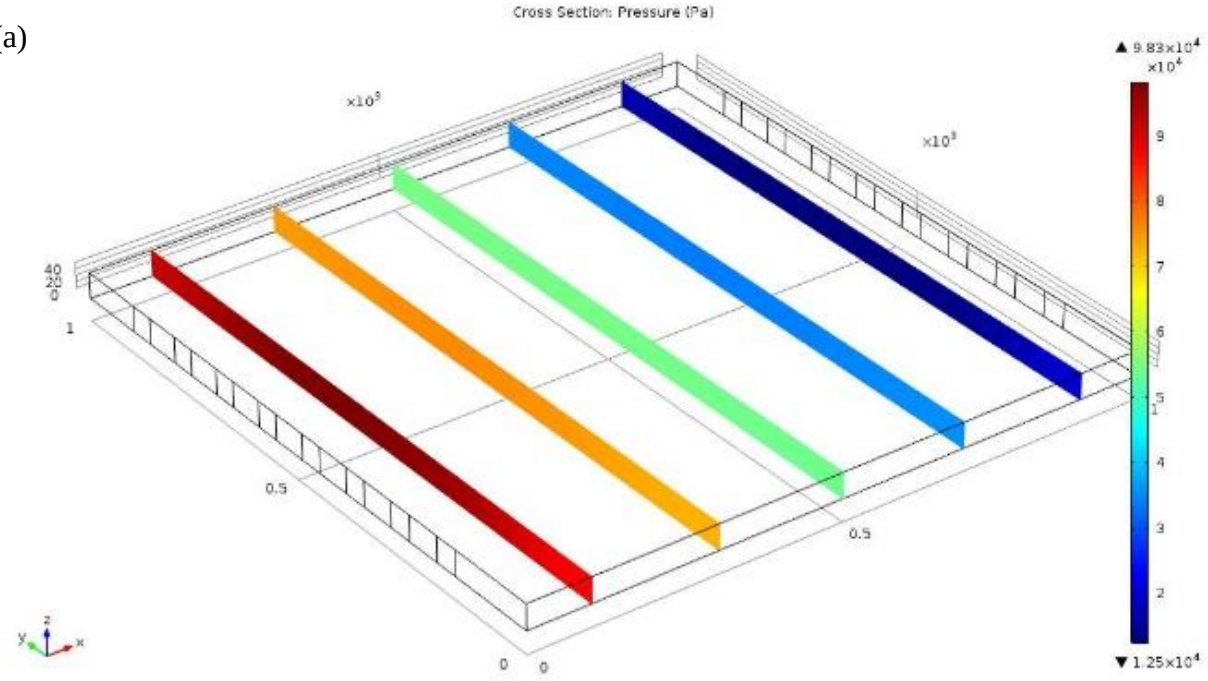

(b)

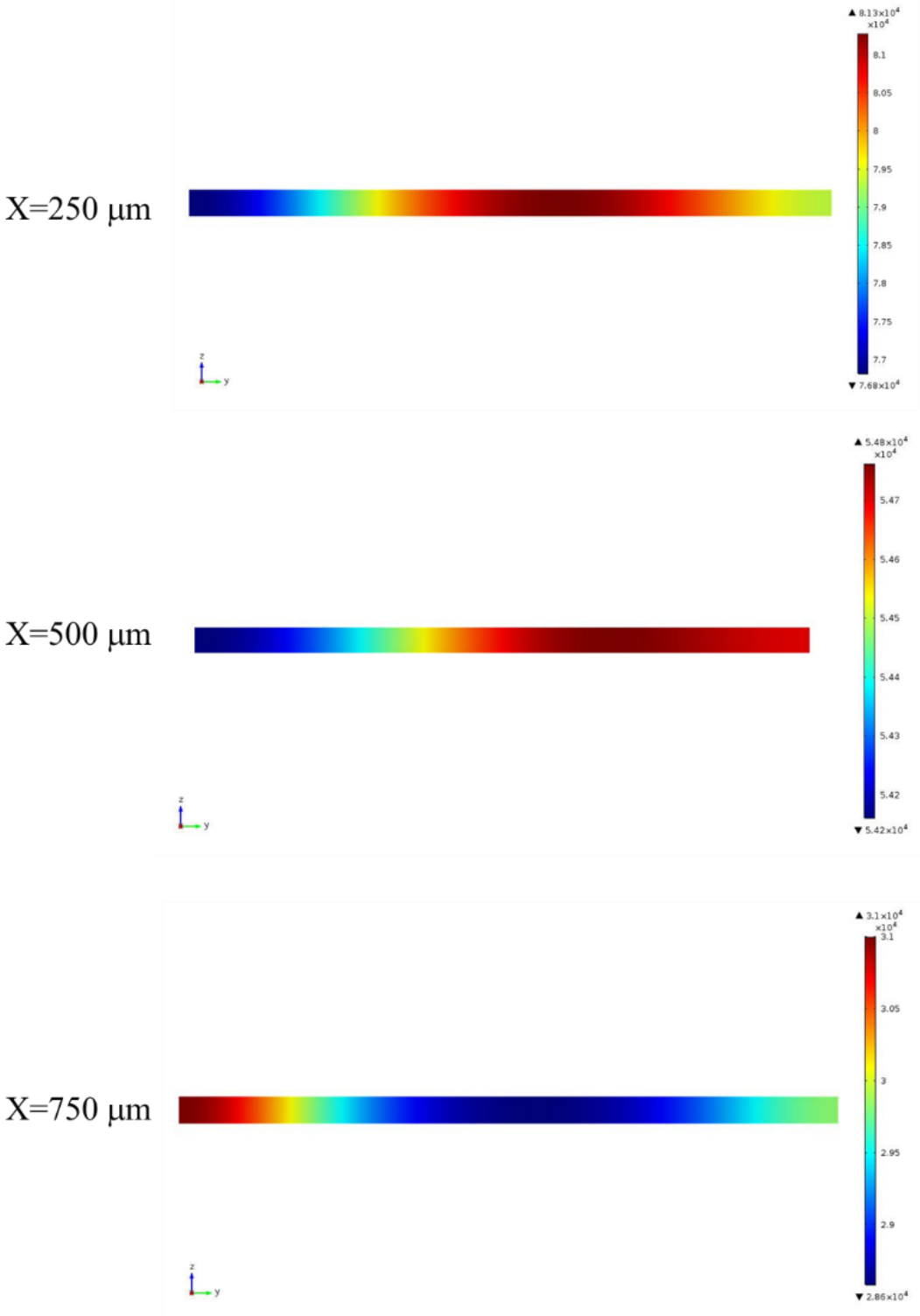

Figure 3.3 (a) The cross-section profile of the pressure inside the microfluidic reactor, uniformly constant at the specific location. Each stripe appears same color at each position along the distance

from the terminal. (b) The YZ cross-section pressure profile in different X positions. The pressure is nearly constant at each position and the pressure is decreasing from 250 μm to 750 μm (i.e., from inlet to outlet direction)

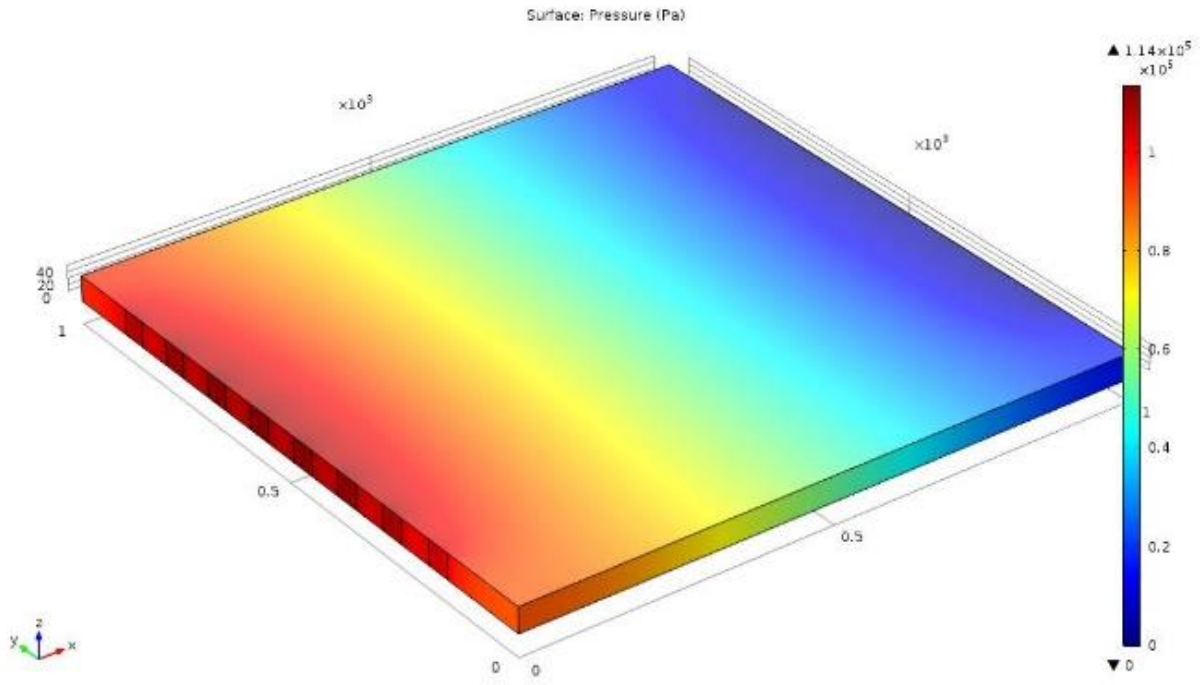

Figure 3.4 Profile of pressure inside the microfluidic reactor. The pressure in the chamber drops continuously along the distance.

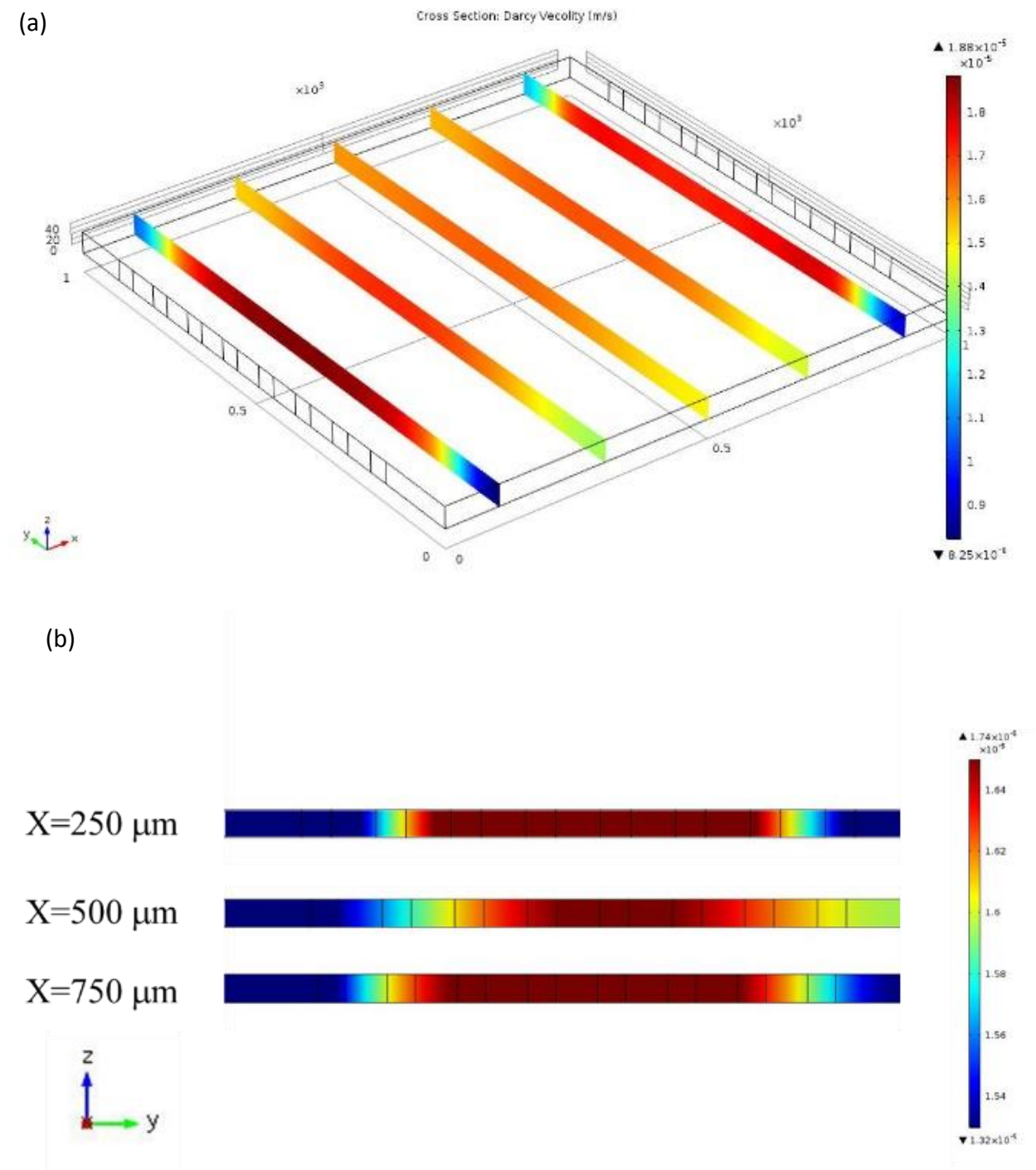

Figure 3.5 (a) Cross-section velocity profile. The velocity of fluid in the central part are relatively larger than at the edge. (b) The darcy velocity profiles at different X positions, which can show

(a)

that the darcy velocity remains uniform steadily. Also, fluid moves fastest in the central region while it is at the lowest speed at the boundaries because of non-slipping effect.

(a)

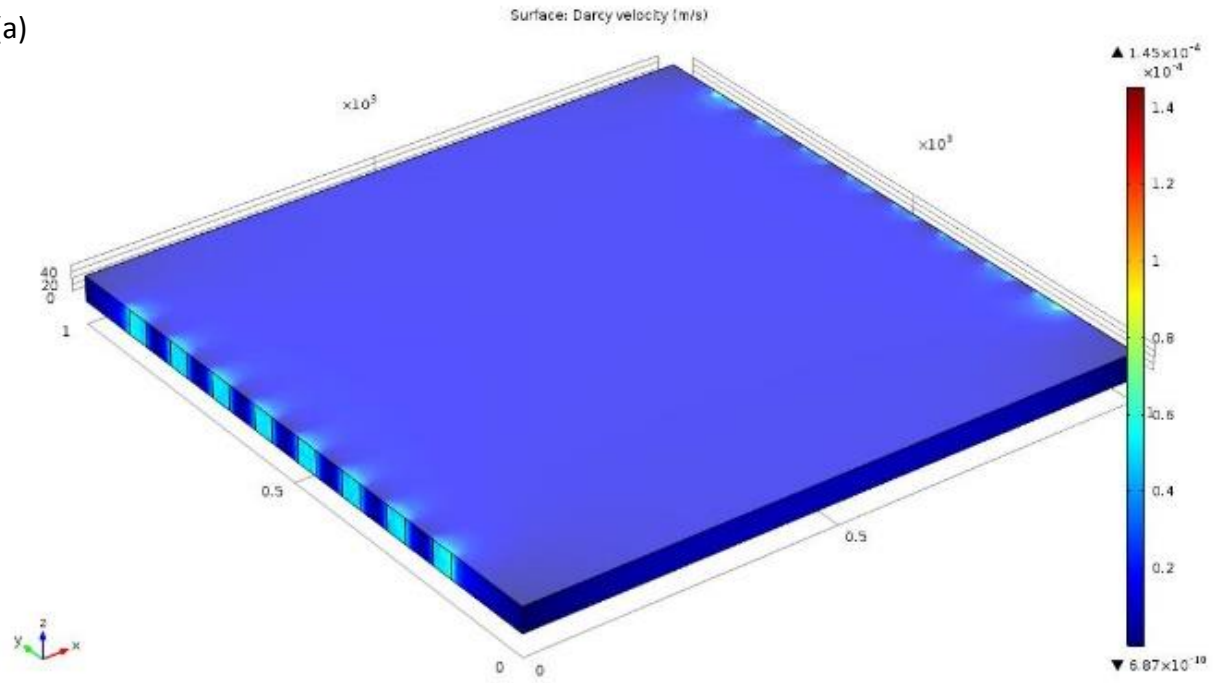

(b)

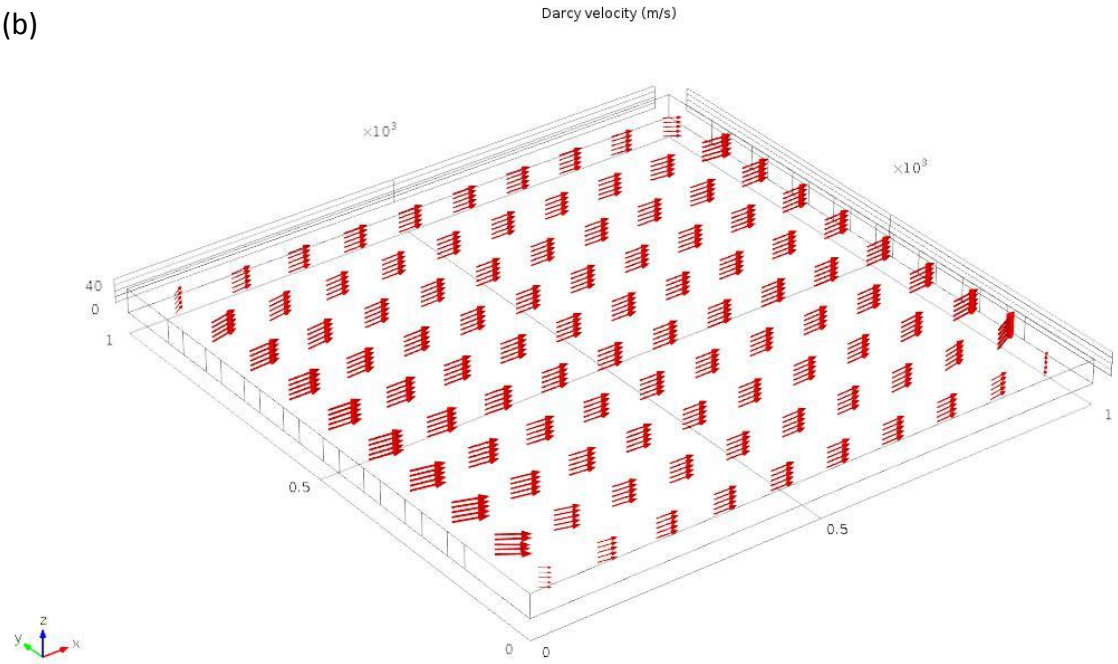

Figure 3.6 (a) Velocity profile inside the microfluidic reactor. The velocity of fluid is zero at the boundary (boundary condition). At the boundary wall, no slipping would occur. It is also noted that the inlets are uniform in velocity. (b) The velocity vector graph shows the major direction component of fluid velocity. It can be seen that no z-component velocity can be seen.

3.5 LSPR simulation result

The structure with the gold nanoparticles (AuNPs) on the surface of TiO_2 should have the LSPR, enabling to absorb part of the visible light region. It was first simulated by FDTD to find the approximate absorption range. By adjusting the wavelength in the visible light region, the graph showing local intensive electric field are attributed to the LSPR phenomenon [37].

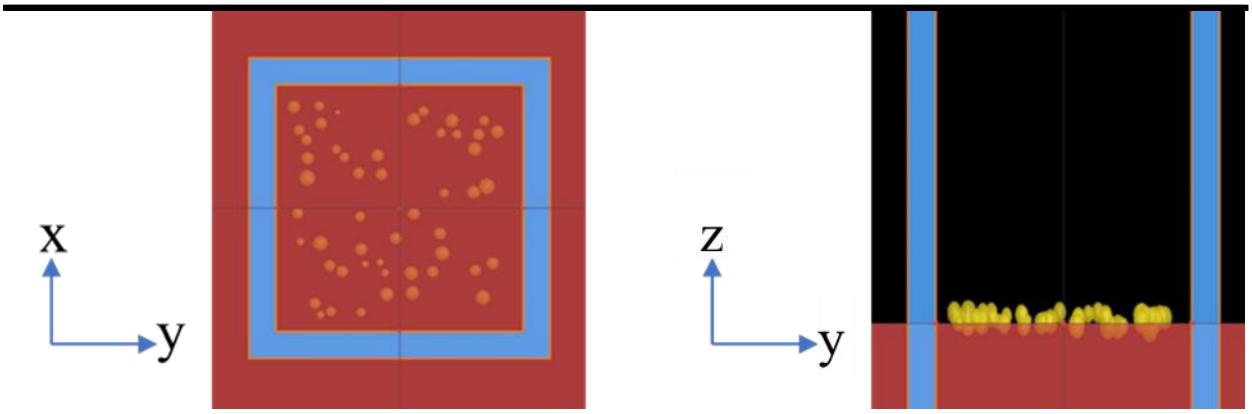

Figure 3.7 The left and right graphs show the xy view and the zy view, respectively. The region of monitor is enclosed by the blue square ring. Inside the region, small yellow balls are AuNPs and the red block is the TiO_2 template [38].

3.5.1 FDTD simulation

The structure of Au/TiO_2 should be simulated by the FDTD. The model is shown in **Figure 3.7**, in which a small local area encloses numerous AuNPs with TiO_2 as the large substrate.

The model uses 50 AuNPs dispersed on the infinitely large TiO_2 template. As the AuNPs are randomly located, there is an additional absorption region ranging from 550 to 625 nm in **Figure 3.8(a)**. In contrast, TiO_2 does not have such a phenomenon. Although the material was prepared first, it is necessary to realize how the AuNPs are put on the TiO_2. TEM results (see **Figure 5.2(e)** and **(f)** in Chapter 5) could not show this interaction. Therefore, three different interactions between AuNPs and TiO_2 were postulated and simulated to represent how AuNPs are formed on TiO_2 in the hydrothermal synthesis. There are all embedded, unembedded and random. Here the "all embedded" state means the AuNPs are fully buried in the TiO_2 template; the "unembedded" state denotes that AuNPs are laid on top of the TiO_2 template; and the "random" state represents the AuNPs are randomly located; some unembedded, some partially embedded

and others full buried. From **Figure 3.8(b)**, the AuNPs unembedded into TiO_2 would have an absorption at 525nm. Moreover, the signal is not intense enough. In the case that AuNPs are partly embedded or partly unembedded, the simulated absorption spectrum is consistent with **Figure 3.8(a)**. The broad absorption in 550-625nm is favorable for photocatalysis [39]. All embedded AuNPs show an intense and board absorption peak from 550 to 700 nm, which is optimal but may not appear completely in the fabricated device. **Figure 3.9** shows the graphs of electric field intensity at five different wavelengths. The bright region shows the high electric field strength due to the LSPR.

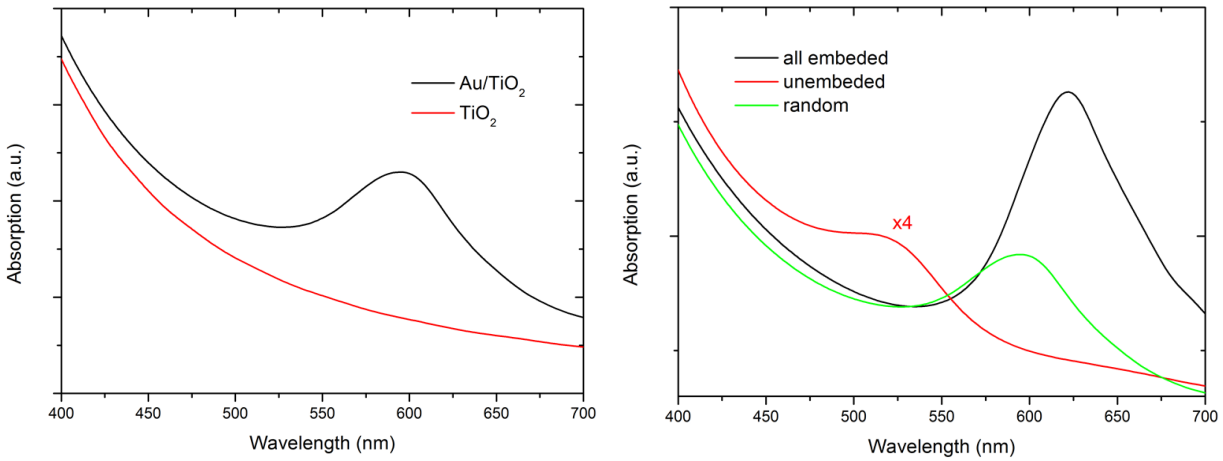

Figure 3.8 (a) The FDTD simulated absorption spectrum of Au/TiO_2 and TiO_2 in visible light region. (b) Absorption spectra of different embedment states the random arrangement is favorable among three cases.

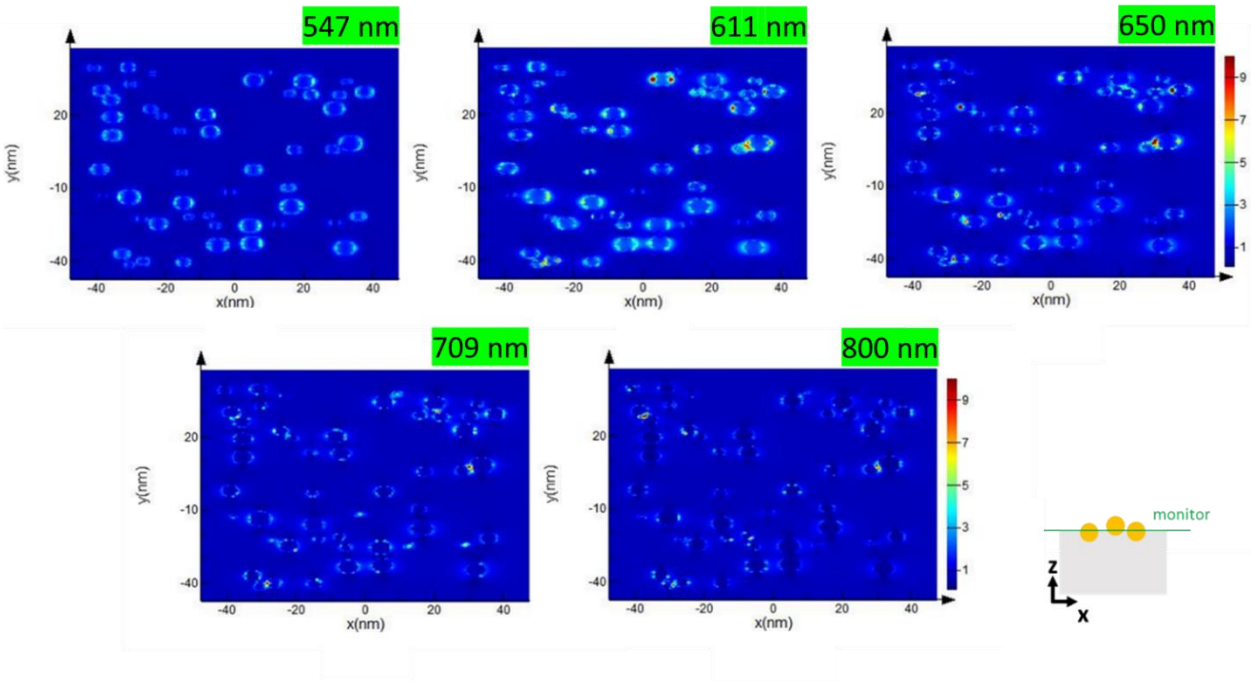

Figure 3.9 Plasmonic effects at five different wavelengths. At 547 nm and 611 nm, the response was more vigorous than that at other wavelengths. Near-field effect could be shown by its bright colour outside the sphere. Therefore, the most apparent response is in 550 to 650 nm.

3.6 Analysis of microfluidic reactor with useful parameters

Finally, the flowing rate should be defined carefully since it is the variable which determines the reaction time (i.e., residence time) of MB inside the microfluidic reactor. Therefore, this parameter affects the photodegradation significantly. The formula to determine the reaction time is [40, 41]:

$$\text{Reaction time} = \frac{\text{Volume of microfluidic reactor}}{\text{Flowing rate}} \quad \textbf{(3.10)}$$

Since the height of the microfluidic reactor enclosing the central chamber is 1 cm × 1 cm × 4 μm, the volume of the microfluidic reactor is thus 4 μl. The small area of the chamber allows a uniform irradiation of light to shine on [29]. Besides, this pattern and dimension were examined

in terms of the flow velocity and the pressure change [42], the results show a uniform flow of fluid and an insignificant pressure drop in the chamber. To achieve the significant color change during photo-degradation, four constant flow rates are chosen to be 2 µl/min, 5 µl/min, 10 µl/min and 50 µl/min. The corresponding four reaction times are 120 s, 48 s, 24 s and 4.8 s.

Due to the Beer-Lambert law [43-45], the absorbance determined by the UV-Vis spectrometer could be correlated with the concentration of species by,

$$A = \log \frac{I_0}{I} = \varepsilon CL \tag{3.11}$$

where A is the absorbance (a.u.), I_0 is the initial light intensity, I is the light intensity after passing through the sample, ε is the wavelength-dependent molar absorptivity coefficient, C is the concentration of the species, and L is the length of the light path through the sample. Assuming the photodegradation of MB in photocatalysis is a first-order reaction whose rate is proportional to the concentration of MB at every instant if the initial concentration of MB is low [46, 47],

$$C = C_0 e^{-kt} \tag{3.12}$$

$$\ln\left(\frac{C_0}{C}\right) = kt \tag{3.13}$$

where C is the concentration of degraded MB (unit: M), C_0 is the initial concentration of MB (around 3×10^{-5} M), k is the reaction rate constant (unit: s^{-1}), t is the time passed (unit: s).

According to **Equation (3.12)**, if the graph of ln (C_0/C) vs. time is plotted, the slope of the linear line is just the rate constant, which means the photodegradation efficiency of different materials under the same conditions [48-50]. Therefore, if the plasmonic effect of Au/TiO_2 is

present such that the overall photodegradation efficiency for the material is enhanced, the slope of the linear line is greater than another material free of LSPR. Besides, the rate constants of photocatalysis found experimentally could be used to compare the superiority of using the stuffed-mode microfluidic reactor in contrast to the film-mode microfluidic reactor [51].

3.7 Summary

In this chapter, two designs of microfluidic reactors are presented, analyzed and simulated. These two designs of the microfluidic reactors have the merits such as an increased SA:V ratio of particles inside the chamber. These packing modes of photocatalysts (i.e., the film-mode and the stuffed-mode) have not extensively utilized in the microfluidic reactor, which represents the uniqueness of this research on this prospect. In the next chapter, the methodology will be presented in detail to discuss the material preparation methods, the device fabrication techniques and the experimental procedures for the microfluidic reactor.

Chapter 4 Methodology

Based on the design and analysis in the previous chapter, this chapter will present all fabrication techniques and experimental procedures of the microfluidic reactor for photocatalytic water purification. The photocatalyst materials in the research are fabricated by hydrothermal synthesis method. Microfluidic reactor is fabricated by a series of standard procedures. After that, the experimental procedure should be standardized for fairly comparison of the efficiencies of photocatalytic materials.

4.1 Materials fabrication

Two samples were prepared for photocatalytic materials, which are TiO_2 and Au/TiO_2. These two materials possess different capabilities to degrade dyes, and it is thus meaningful to examine their function in the microfluidic reactor. TiO_2 and Au/TiO_2 can be prepared by a series of procedures, such as hydrothermal synthesis. Normally, two share similar structure because Au/TiO_2 will be fabricated by the precursor for TiO_2.

4.1.1 TiO_2

The fabrication procedure of TiO_2 is illustrated in Figure 4.1. For the synthesis of mesoporous TiO_2, the mixture of 350-ml isopropyl alcohol, 300-μl diethylenetriamine and 12.5-ml titanium tetraisopropanolate was placed in the 500-ml container. It was stirred for more than 5 mins. A magnetic stirrer was evacuated from the mixture, and then put in an autoclave at 200 ^oC for 48 hr. The sample was transferred to the centrifuge tube for being centrifuged at 9000 rev for 10 mins.

The next procedure is removing the top clear layer of residue solution and putting in the ultrasonic bath and centrifuge. This process should be repeated three times. Then, the sample could be extracted and examined by microscope. A top layer of residue solution was removed for easy drying before putting the remaining solids into a clean container with aluminum foil covering the opening. Finally, the sample was put in the Muffle furnace at 400^{o}C for 1 hour to collect mesoporous TiO_2.

4.1.2 Au/TiO_2

Au-decorated TiO_2 has the similar synthesis procedure. In **Figure 4.1**, the first step is to make mesoporous TiO_2 samples by the method mentioned above. 100-mg TiO_2 was collected and filled with 20-ml ethanol in a centrifuge tube. Then the sample was put in an ultrasonic bath. After the ultrasonic procedure, a stirrer was put into the container for stirring. During stirring, 200-µl thioglycolic acid was added inside the mixture by covering container for more than 3 hours. The stirrer was removed before and the mixture was centrifuged at 9000 rev for 10 mins. The top clear layer of the solution was removed and added with ethanol for centrifuging. The above process was repeated 2 times but ethanol should be added less for the last time. Aluminum foil was used to shield light and the sample was stirred for more than 3 hours. During stirring, 1 mM 20-ml Chloroauric Acid was added. Then, aluminum foil was taken off, centrifuged at 9000 rev for 10 mins. After clearing the top layer of clear solution, ethanol was added to help disperse sample in the ultrasonic bath. During the period of a stirrer added to physically stir the mixture, 100mg Sodium borohydride which was dissolved in water was dropped into the container. The container should not be covered because hydrogen gas would make the cover collapse. After stirring for 5 to 10 minutes, the sample was centrifuged with 9000 rev for 10 mins. After clearing the top layer

of solution, adding ethanol in the ultrasonic bath several times was done before washing by deionized water for 1 to 2 times. Finally, the sample was dipped for microscopic picture and put it in an oven for drying.

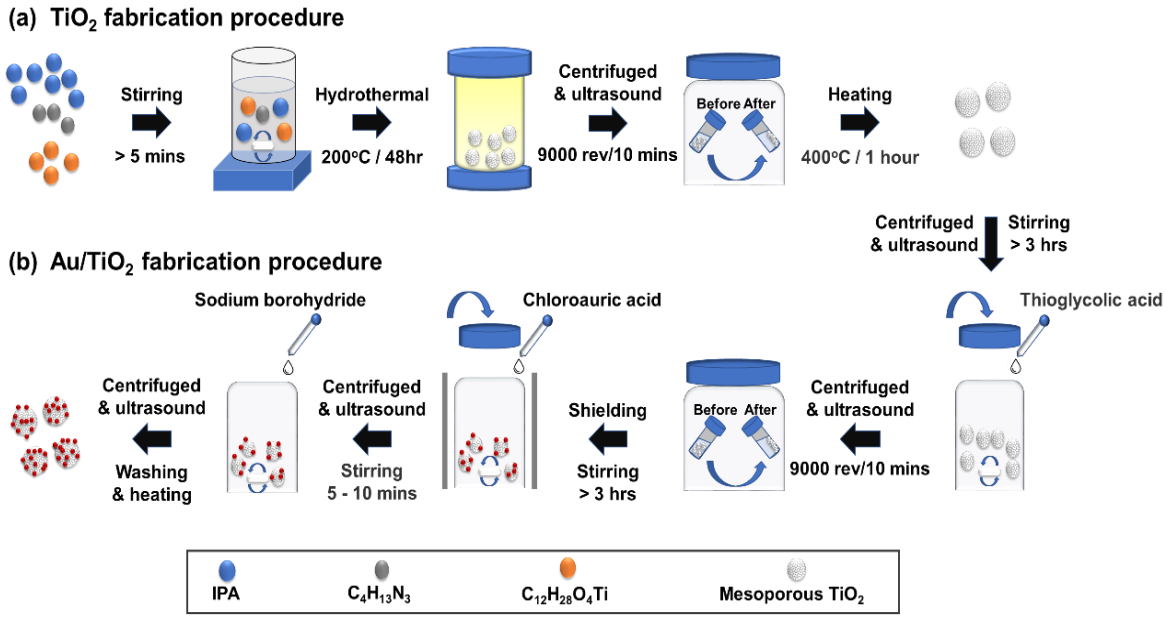

Figure 4.1 TiO_2 and Au/TiO_2 were fabricated by hydrothermal synthesis [52], followed by a series of centrifugation and ultrasonic to make sample with high purity. During stirring, some precursor for making Au/TiO_2 were added.

4.2 Microfluidic reactor design

The schematic design of the microfluidic reactor is illustrated in **Figure 4.2**. The device consists of three main components: an inlet, a central reaction chamber, an outlet. In between every duct and chamber are the capillary channels, which facilitate the uniform flow of indicator solution through the central chamber. The inlet and outlet are for the injection of fresh dye and the collection of degraded dye, respectively. The chamber is fabricated with the specific dimension (1 cm × 1cm × 40 μm) to confine the photocatalytic reaction under light, as shown in **Figure 4.2(c)**.

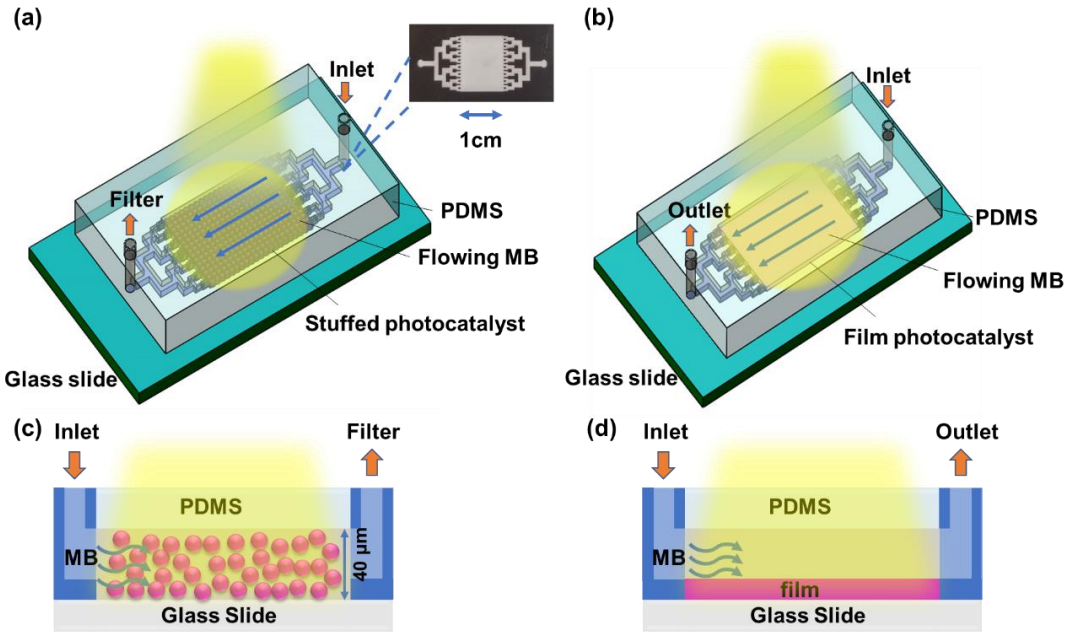

Figure 4.2 (a) The schematics of stuffed-mode microfluidic reactor in which photocatalyst particles are packed inside the chamber. (c) Cross-sectional view. The filter (pore size = 0.22 µm) connected via the outlet in the stuffed-mode microfluidic reactor prevents the loss of tiny photocatalysts, immobilizing particles for efficient photocatalytic reaction. (b) Film-mode microfluidic reactor by depositing a thin film on the glass slide first and by then capping a PDMS slab on the top. (d) Cross-sectional view of the film-mode microfluidic reactor.

The actual dimension of the microfluidic reactor is measured by light microscope and surface profiler. In **Figure 4.3**, the channel width becomes thinner from the inlet to the chamber. It could form many fine flows when entering the capillary channel.

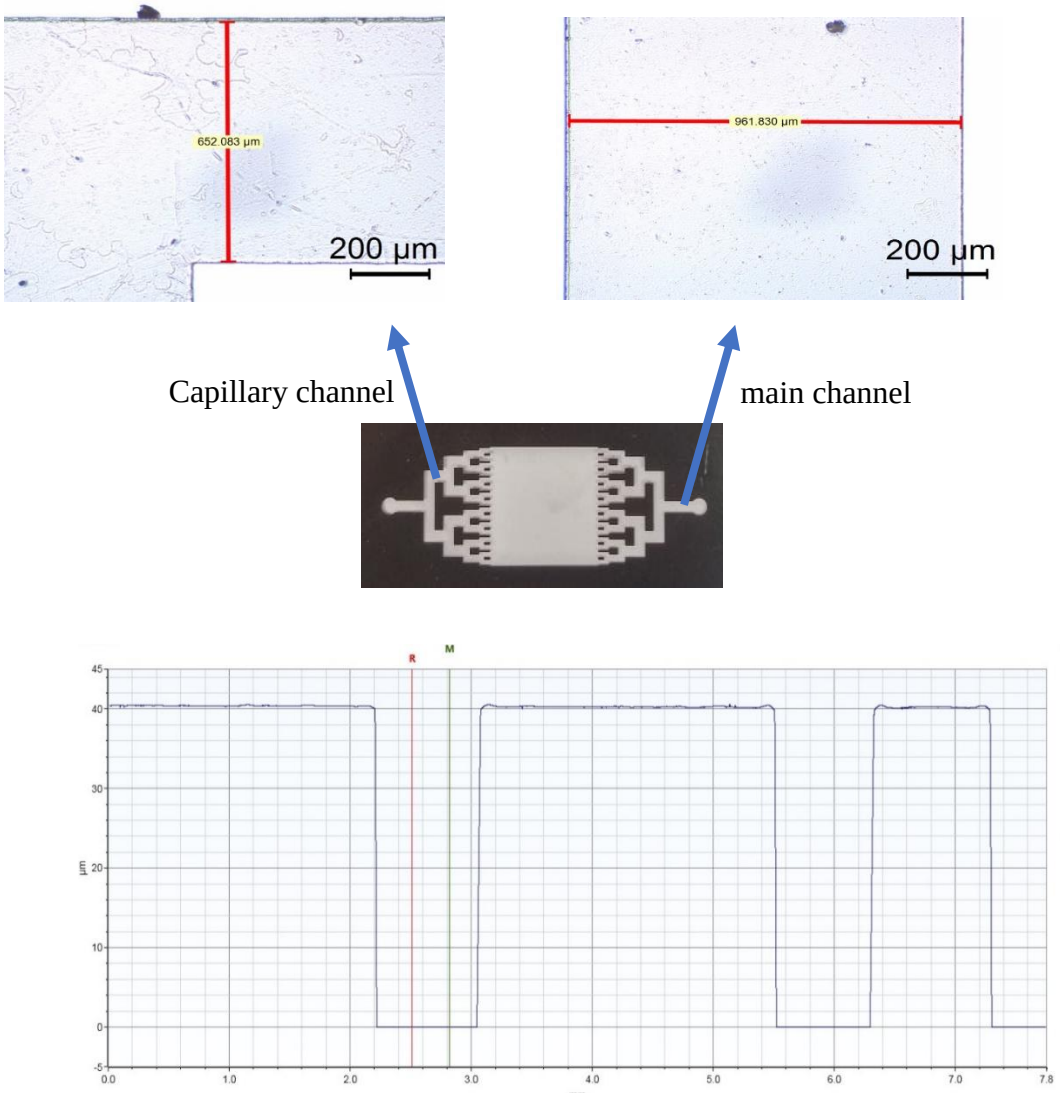

Figure 4.3 Dimensions of microfluidic reactor. The widths of main channel and capillary channel are 1 mm and 0.65 mm, respectively. The height of photolithographic pattern is 40 µm relative to the reference plate.

The bottom of the microfluidic reactor is a glass slide, which is attached to a PDMS slab by plasma bonding. PDMS is a flexible material [53] and has been extensively utilized in microfluidic device. Its relatively low Young's modulus makes it suitable for microfluidic reactor.

Also, it is transparent and inert under ambient condition, allowing for chemical reactions like water purification under sunlight.

4.3 Microfluidic reactor fabrication

The device is composed of a PDMS slab (main material) and a glass slide (substrate). First, a clean silicon wafer (4-inch) was prepared after being immersed into acetone, IPA and water inside the ultrasonic bath. After drying and cleaning by plasma cleaner, 4-ml negative photoresist SU8-2050 was added onto the clean silicon wafer. SU-8 2000 is a high contrast, epoxy-based photoresist that the film thickness of 1 μm to 100 μm could be achieved by spin coater. It was subsequently span coated by two successive steps with spinning speed to deposit a uniform thickness of photoresist (~40μm). The first step is 500 rpm for 30s for coarsely spreading photoresist while the second is 1500 rpm for 60s for finely controlling the final photoresist thickness. Soft bake at 65°C and hard bake at 95°C should be done to make the photoresist hard before the UV exposure. The whole sample with designed pattern photomask was put on the platform for UV exposure in 45 seconds which makes the transparent part of the photoresist hardened [54]. Followed by post bake at 65°C and 95°C respectively for the formation of cross-linkage of photoresist, the silicon wafer can be immersed inside the SU-8 developer for 10 mins. After drying by nitrogen gas, the silicon wafer with photoresist pattern was completed [53, 55].

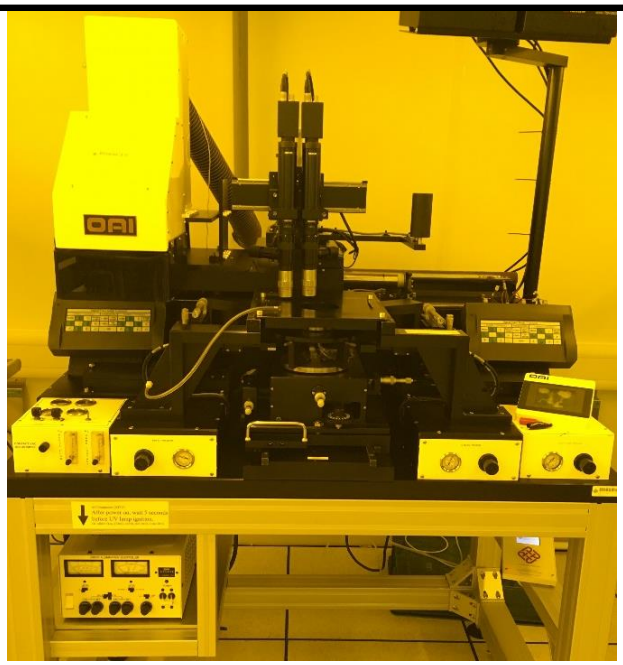

Figure 4.4 Photolithographic setup (OAI 800 Contact Aligner) primarily consists of the substrate for placing the sample and the UV lamp source. They could be controlled by applying vacuum to the platform and by adjusting the irradiation time of UV in the control panel.

Table 4.1 All steps for making a 40-μm thick photoresist layer on the silicon wafer. Here, rpm means revolution per minute. The deposition of SU8-2050 needs two spinning steps following by baking for hardening photoresists. The UV exposure time determines the hardening capacity of photoresist. The post-baking further strengthens cross-linkage, the unused part of photoresist will be removed by SU8-2050 developer.

Spin speed (rpm)	**Prebake @65˚C (minute)**	**Softbake @95˚C (minute)**	**UV exposure (second)**	**Post-bake @65˚C**	**Post-bake @95˚C**	**Develop (minute)**
1st: 500 2nd: 1500	10-15	30	45	1	10	10

The fabrication procedures of PDMS slab are shown in **Fig 4.5**. PDMS prepolymer and solidifying reagent were mixed in 10:1 ratio [50]. After stirring for 10 mins, PDMS was poured on the silicon wafer with pattern and put in the pump for degassing. Gas bubbles on the microfluidic reactor may hinder the light penetration through the reaction chamber. PDMS with the silicon wafer was then put into the oven for gentle warming. After PDMS was hardened, the PDMS slab was cut for bonding onto a clean glass slide [55]. Finally, inlet and outlet were punched.

At the final stage, PDMS should be covalently bonded onto the glass slide to form a sealed reactor chamber. For the PDMS bonding, oxygen plasma, which consists of a medium of positive and negative charges, helps transform the Si-CH3 into Si-OH functional group [56]. Therefore, the PDMS slab could be bonded onto the glass slide via the formation of plasma bonding of two surfaces [57]. The chamber inside the microfluidic reactor should be evacuated with air until the pressure reached 200 mTorr. Then, oxygen gas was pumped into the chamber to the level of 400 to 500 mTorr for several minutes, followed by turning on the RF level from “LOW” to “HIGH” to excite oxygen plasma. After 3 minutes, the gas supply and equipment were turned off before two bonding sides were put together [56]. Exciting the bonding surface too long would cause adverse effects, such as the roughening of the surface, which would make bonding more difficult.

After pressing the PDMS and the glass slide, a strong and permanent Si-O-Si link network was formed to withstand the pumping pressure inside the chamber. The device was generally fabricated according to the following procedures.

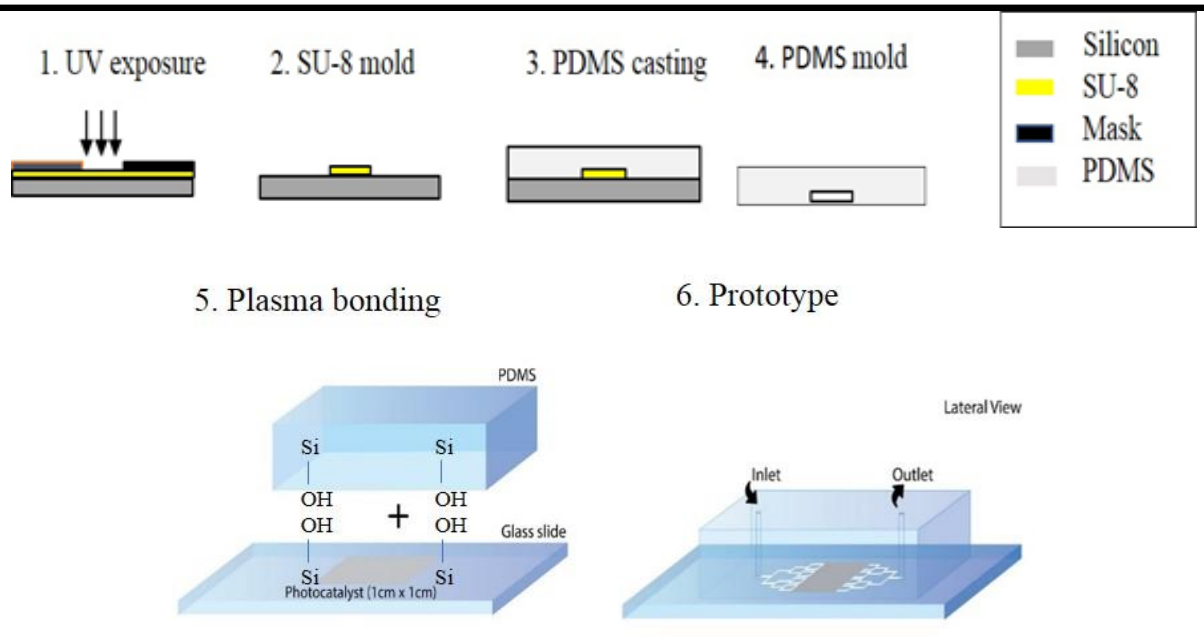

Figure 4.5 Photolithography of SU-8 photoresist, putting PDMS onto the patterns for prototyping the PDMS slab with the desirable pattern (1-4) [58]. PDMS slab was bonded onto the glass slide via the bonding of two bonding surfaces by plasma cleaner. The plasma bonding is a kind of chemical bonding which helps attach two objects and thus withstand the fluidic pressure in the chamber (5-6).

4.4 Experimental procedure

The major goal of the thesis is to evaluate the contribution of high SA:V of photocatalysts inside the microfluidic reactor. Initially, three modes were designed for optofluidic photocatalysis, namely suspension-mode, film-mode and stuffed-mode. In **Table 4.2**, it lists the respective advantages and drawbacks of each mode. The goal and feature of the experiments are listed in the following diagram. However, the microfluidic reactor usually manipulates the tiny amount of sample, therefore film mode and stuffed mode will be highlighted more.

Table 4.2 Optofluidic reactor could be usually categorized into three modes, namely suspension, film and stuffed. Each one has unique benefit and drawback for experiment. Nevertheless, film mode and stuffed mode could be exploited in microfluidic reactor for fostering the efficiency of various chemical reactions.

	Suspension-mode	**Film-mode**	**Stuffed-mode**
Advantages	- Easy testing - Large SA:V - Short diffusion length - Fast reaction	- Easy fabrication - Low pressure drop - No need to recycle	- Short diffusion length - Large SA:V - Fast reaction - No need to recycle
Disadvantages	- Need stirring - Difficult to recycle - Non-uniform photon transfer	- Long diffusion length - Drop-off of photocatalyst	- High pressure drop

4.4.1 Suspension-mode reactor

The suspension-mode [59, 60] reactor is the easiest one for comparing the photodegradation efficiency of different photocatalysts under visible light. A fixed amount (~0.5-g) of photocatalysts (e.g., TiO_2 or Au/TiO_2) was stirred on the container with the same amount (~5-ml) of MB under light. Dark reaction, which allows the MB to fully adsorb the photocatalyst, was carried out before the light was turned on [61]. However, since there were experimental constraints (i.e. light penetration through the mixture solution and scattering of light by the solution surface.) which hindered the accuracy of the results, this part would not be studied further.

4.4.2 Film-mode microfluidic reactor

Before depositing a film on the glass substrate, a mixture of suspension was made. 0.2-g ground sample powder of TiO_2 or Au/TiO_2 was dispersed slowly in 2-ml deionized water, followed by adding 6.67-µl acetylacetone solution which helps the aggregation of the particles during stirring. 3.33-µl Triton X-100 was added into the mixture to help prevent agglomeration of colloid on the glass substrate. Finally, 0.02-g polyethylene glycol (PEG) was put and stirred over a night [19].

The film was rolled by glass roll with a scotch tape covering the edge of the glass slide and sandwiched by the glass slide (bottom) and the PDMS slab (top). The schematic of the film-mode microfluidic reactor and its cross-section view are shown in **Figure 4.2(b) and 4.2(d)**. The photocatalytic efficiencies of TiO_2 and Au/TiO_2 under visible light irradiation were examined by the degree of decomposition of MB, which could be inferred by its gradual color change. First, MB was pumped into the microfluidic reactor via the inlet. Before the data were collected from every run of the experiment, MB needed to be injected by the syringe pump with a moderate low flow rate (i.e 5 µl/min) without light. This process is known as dark reaction, ensuring the film photocatalysts to be adsorbed by MB molecules and be saturated finally. The light source, which is a tungsten light lamp, was subsequently turned on to irradiate the central area (1 cm × 1 cm) of the microfluidic reactor. Four data points were respectively collected for four different flow rates [62]. In between every run of flow rate, the adsorbed residue MB would be drained away by deionized water with the irradiation of UV-light for making control experiment [63]. Then, it started with another dark reaction before the test of another.

4.4.3 Stuffed-mode microfluidic reactor

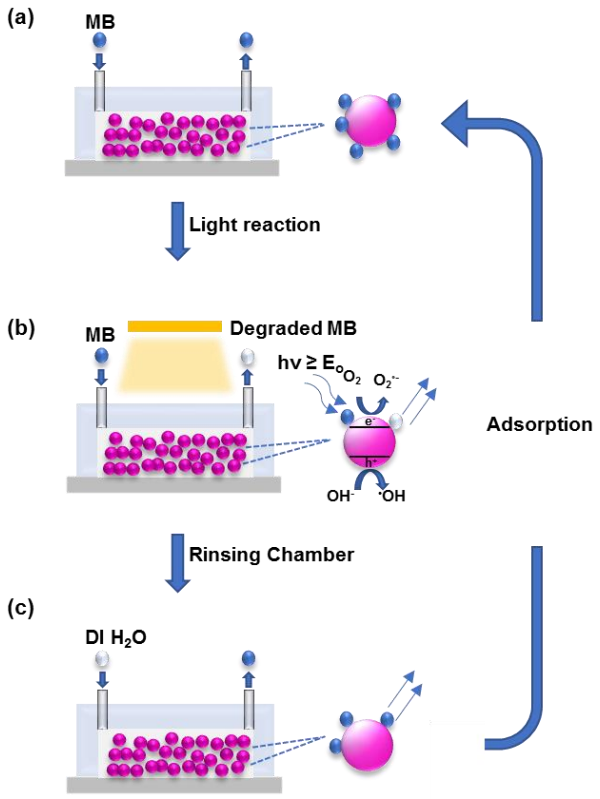

Figure 4.6 (a) In each experimental run, MB was pumped into the chamber for dark reaction. (b) Then the photocatalysis of MB was initialized by light and photocatalysts. (c) All absorbed MB after photocatalysis would be rinsed to prepare for the dark reaction in next cycle [64].

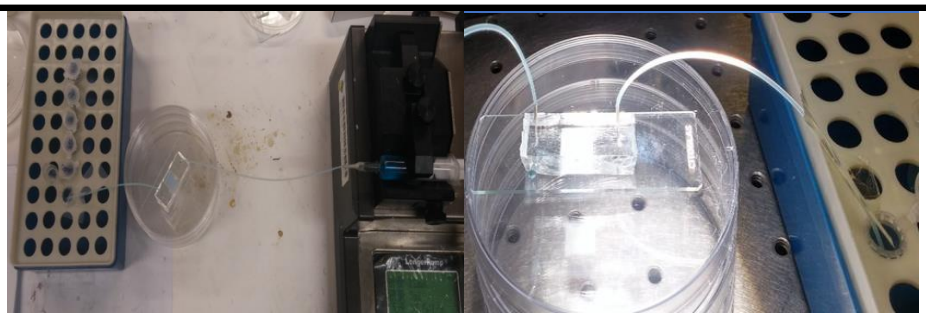

Figure 4.7 Experimental setup. Dark reaction in every cycle (Left). Light reaction, that is, the reactor is irradiated for photocatalytic degradation at different flow rate (Right). The degraded sample was collected and tested for its absorbance.

The operation and experimental setup are illustrated in **Figure 4.6 and 4.7**. This mode is a novel design of microfluidic reactor for comparing the photocatalytic efficiency of materials [65, 66]. It is advantageous over the other reactor designs due to its considerably high SA:V of photocatalysts inside the chamber. The efficiency of the microfluidic reactor for degrading MB was investigated with the same method. First, 0.1-g TiO_2 or Au/TiO_2 were ground and mixed with 1-ml ethanol (10wt% in the mixture) in ultrasonic bath for one hour. The mixture was then manually injected into the microfluidic reactor chamber by syringe for several times until the microfluidic reactor appeared uniform milky white for TiO_2 and uniform dark pink for Au/TiO_2. For the fabrication of this reactor, prior oxygen plasma treatment was reported to reduce the hydrophobicity of a sealed PDMS microchannels [67-69]. Ethanol acted as a medium carrier to bring and immobilize TiO_2 into the reactor. The subsequent procedures for photodegradation test were carried out repeatedly like the film-mode microfluidic reactor.

4.5 Summary

This chapter elaborated the fabrication procedures of materials and microfluidic reactor. Mesoporous TiO_2 and Au/TiO_2 were prepared by the hydrothermal synthesis. Then, microfluidic reactor was fabricated by a series of procedures as follows:

(1) Making a photolithographic pattern using SU-8 on a silicon wafer.

(2) Fabricating a PDMS slab by replication from the SU-8 mold.

(3) Forming a microfluidic reactor by plasma bonding the PDMS slab onto the glass slide.

Besides, every run of experimental data should be controlled carefully to ensure the reliability and repeatability of data. All experimental conditions should be kept the same under all circumstances. Therefore, every adsorbed MB molecule should be rinsed by pumping deionized water followed by re-adsorption of MB on TiO_2. Careful experimental procedures should be followed in the experiments of microfluidic reactors to compare their efficiencies, which will be conducted in the next chapter.

Chapter 5 Experimental Result

Based on the materials and the devices developed in the previous chapter, this chapter will characterize the material properties and test the device performance. The former aims to find why Au/TiO_2 is superior to TiO_2 and the latter part will experimentally show why Au/TiO_2 in the microfluidic reactor has higher photodegradation efficiency than TiO_2.

5.1 Characterization of structural form of materials

The two most common phases of TiO_2 are anatase and rutile. These two forms have different crystal structures and different band gap energies (ΔE = 3.2 eV for anatase, ΔE = 3.0 eV for rutile) [70, 71], and may result in different photocatalytic efficiencies. The XRD patterns are plotted in **Figure 5.1**, in which the marked peaks will agree with the corresponding intensity peaks in the literature data. Both show three distinct peaks A (101) at 25^o, A (103) at 36^o and A (200) at 46^o [72, 73]. These suggest that the sample primarily consists of anatase phase instead of rutile phase.

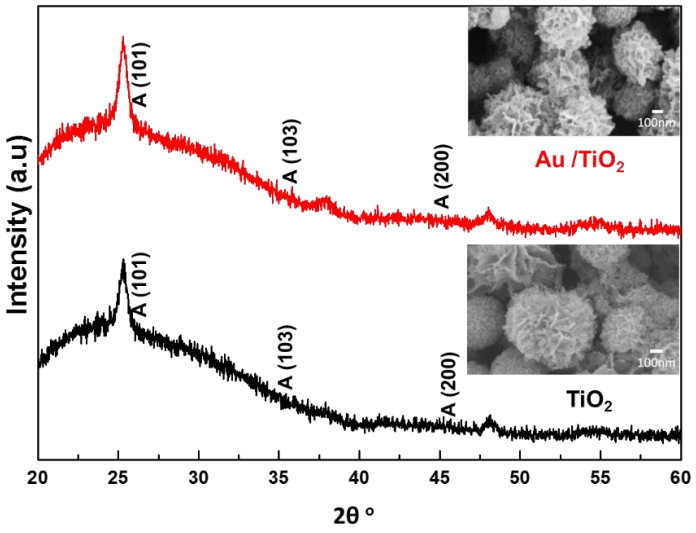

Figure 5.1 XRD patterns of Au/TiO_2 (marked in red line) and TiO_2 (marked in black line). The most detectable polymorph of TiO_2 is anatase with its Miller indices of the inter-plane in the crystal. The insets show the mesoporous surfaces of Au/TiO_2 and TiO_2 taken by scanning electron microscope (SEM).

Anatase TiO_2 may have better photocatalytic activity than rutile. According to the literature data, anatase generally has a larger band gap than rutile. Luttrell et al. proposed that its valence band maximum is raised to a higher energy level relative to the redox potentials of adsorbed molecules [74]. Anatase has more oxidative power, which has more tendency to leave electrons when anatase reacts with the adsorbed species.

Another reason is that anatase exhibits a smaller indirect band gap than its direct band gap, the lifetime of the charge carrier is longer than the time in the direct band. If the electron-hole pair excited in semiconductor photocatalysts has a longer lifetime, it is more likely for these charge carriers to take part in the surface reaction [74]. However, rutile phase has similar

indirect and direct band gap, which implies that the significance of long lifetime of the charge carrier is not the major factor[75].

It is consistent with the finding that AuNPs on anatase TiO_2 are about two orders of magnitude more active than AuNPs of a similar size on rutile TiO_2 [76]. The experiment for comparing the efficiencies of the two polymorphs is hydrogen production from ethanol and Au/TiO_2, which could be linked to the recombination rate of excited hole and electron [76]. Therefore, it provides solid experimental proof of the higher photocatalytic performance of Au/TiO_2.

5.2 Morphological and compositional studies

The prepared TiO_2 conducted in this experiment is preferably mesoporous (pores with diameters between 2 and 50 nm) because it offers high SA:V. It is reported that the rough and mesoporous photocatalysts could enhance photocatalytic activity since they provide more channels or effective adsorption sites for dye molecule [77, 78] and increase the mass transfer rate [79]. Also, the diameter of TiO_2 was found to range approximately from 300 to 400 nm, the overall structure of an isolated photocatalyst may appear like a large ball decorated with numerous dots on its surface. This structure could be close proximity to reactant fluids for photocatalytic reaction [80].

To visualize the AuNPs, TEM with EDX (energy-dispersive X-ray spectroscopy) is used for high resolution imaging. The results are shown in **Figure 5.2**. It can be seen from **Figure 5.2(a)** to (b) that the TiO_2 nanoparticle is almost spherical and has a lot of fur-like substructures, which is beneficial to the photodegradation. **Figure 5.2(c)** shows the lattice constant of TiO_2 is 0.35nm, matching that of anatase phase. As can be seen from **Figure 5.2(d)-(e)**, many small AuNPs decorate the large TiO_2 sphere (~350nm). In **Figure 5.2(e)** and **(f)**, AuNPs are spherical in shape

and around several nanometres in diameter. There are 50 AuNPs in **Figure 5.2(e)**. The histogram inserted in **Figure 5.2(e)** shows the AuNPs size is in the range of 2 – 6.5 nm, with most of them at 3.5 nm. The random size of AuNPs abroad plasmonic absorption peak which is favorable for the photocatalysis using sunlight. **Figure 5.3** shows the element compositions of TiO_2 and Au/TiO_2. It is seen from **Figure 5.3(a)** that TiO_2 consists of only Ti and O atoms, and from **Figure 5.3(b)** that Au/TiO_2 has Au atoms.

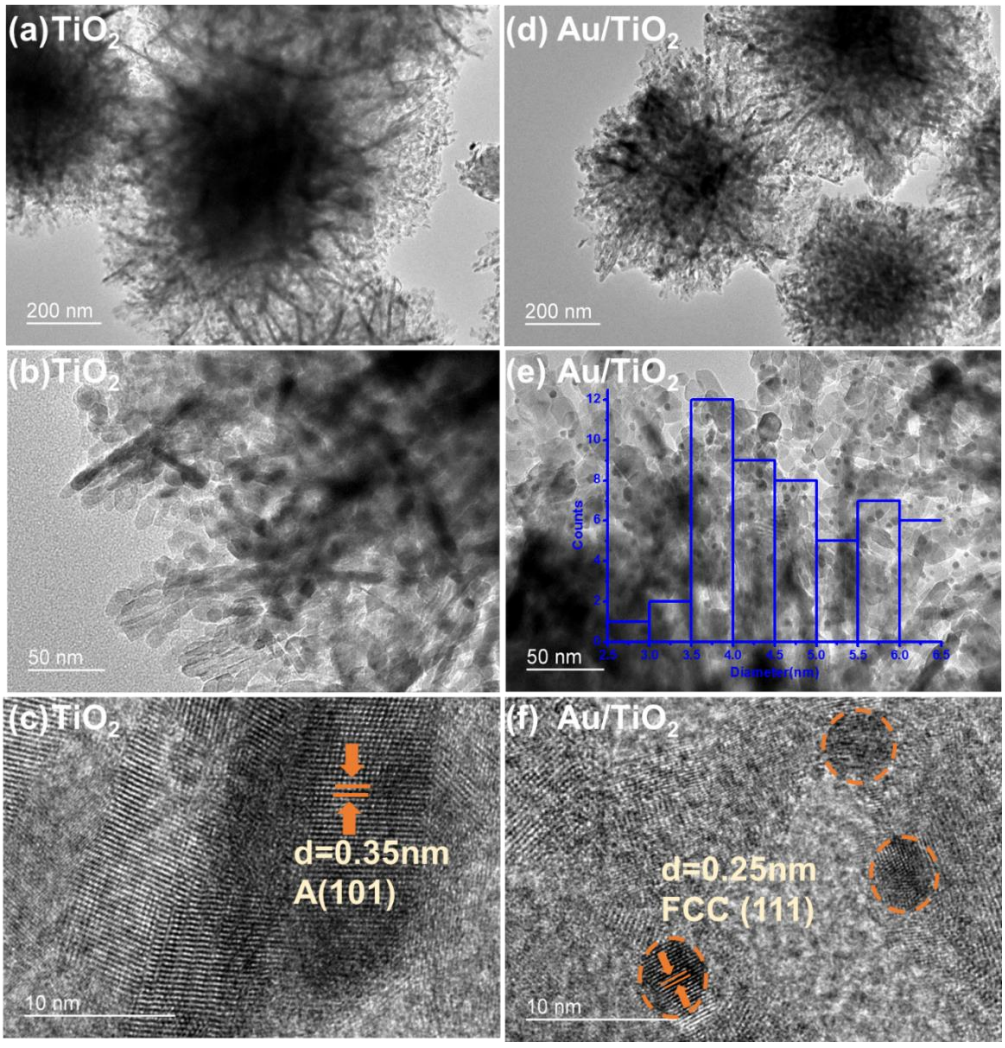

Figure 5.2 (a) Bright-field TEM reveals there is no existence of AuNPs on TiO_2 at all. (b) Only many pieces of TiO_2 grains are observed. (c) The magnified micrograph of TiO_2 shows the lattice

constant of its anatase crystal structure. (d) The Au/TiO_2 cluster is spherical in shape. (e) Au/TiO_2 shows numerous AuNPs dispersed on the TiO_2 surface. The inset is the size distribution histogram of 50 AuNPs, over the range of 2 – 6.5 nm and mostly at 3.5nm. (f) Round-shaped AuNPs indicated by orange dash line are distributed near the Au/TiO_2 clusters with its face-centered cubic structure.

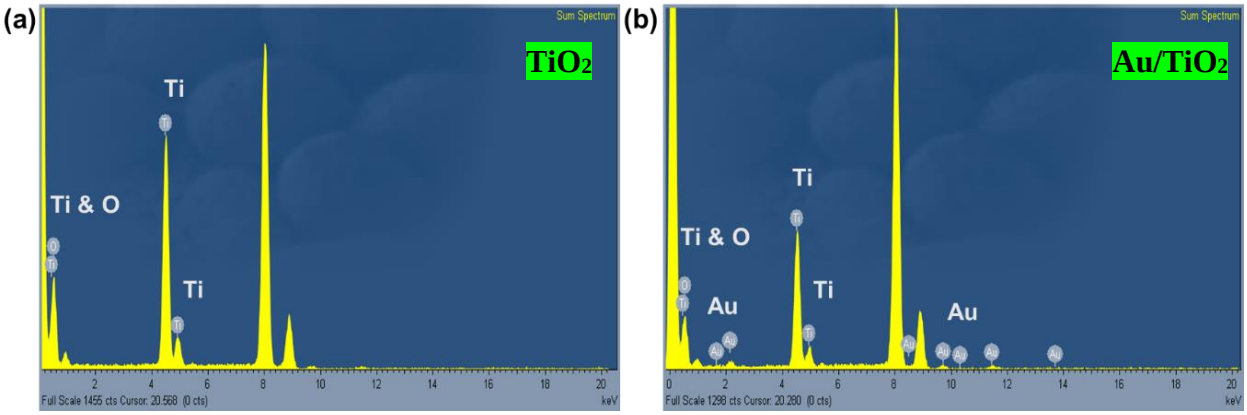

Figure 5.3 Elemental analysis further adds more information on what elements are included in sample. (a) TiO_2 is composed of titanium and oxygen atoms only. (b) Some gold peaks appear in Au/TiO_2.

The elemental analysis in **Figure 5.3** shows the compositions of sample materials, however, it does not show that AuNPs are dispersed or interacted with TiO_2.

TEM mapping in **Figure 5.4** could provide the supportive result. Taking a cluster of Au/TiO_2 as a central part, AuNPs are dispersed in the vicinity of TiO_2 uniformly. Therefore, AuNPs could physically interact with TiO_2 to provide a drain for charge carrier transport [81]. Here, TiO_2 could act as electron acceptor if the excited electron from AuNPs could transfer to the conduction band of TiO_2.

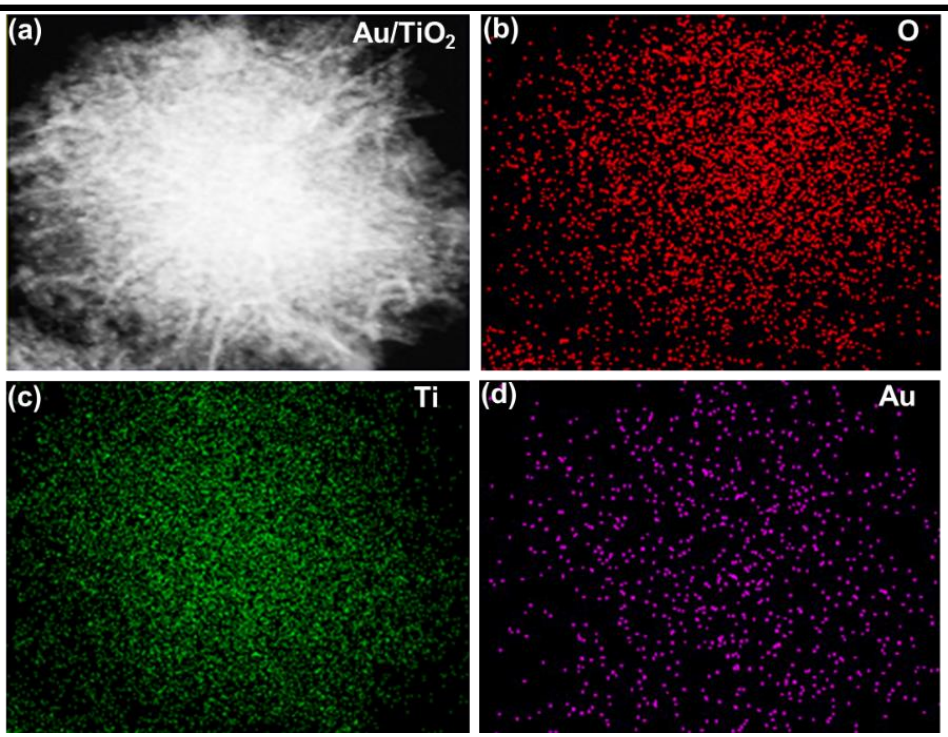

Figure 5.4 Elemental mapping of each constituent element in the sample, showing even distributions of (a) Au/TiO_2 cluster, (b) oxygen atom, (c) titanium atom and (d) gold atom.

5.3 Adsorption spectrum of photocatalysts film

This experiment aims to prove that plasmonic photocatalysts could benefit the photodegradation efficiency significantly. In **Figure 5.5(c)**, the characteristic absorption peak of MB at 664 nm drops with slower flowing rate. It can be used to quantify the relationship of flowing rate with photodegradation efficiency under visible light.

The measurement setup and results of the MB concentrations at different flow rates are shown in **Figure 5.5**.The setup is Shimadzu UV-2550 UV-Vis photo-spectrometer as shown in **Figure 5.5(a)**. As schemed in **Figure 5.5(b)**, the mechanism is basically based on the fact that electron transition in atom are excited by quantized energy of photon during absorption of light

[82]. First, two cells act together for baseline. Then, the reference cell provides the intrinsic absorption of the background, and the sample cell contains the targeted species. As shown in **Figure 5.5(c)**, the absorbance of MB in visible light region is prominent at 664 nm. The spectra show that when the flow rate decreases, the adsorption peak drops, the photodegradation efficiency of MB due to photocatalytic materials is higher [83]. **Figure 5.5(d)** shows the photos of the photodegraded MB solutions. It is seen that the solution color changes from blue to very light blue when the flow rate drops from 50 μm/min to 2 μm/min.

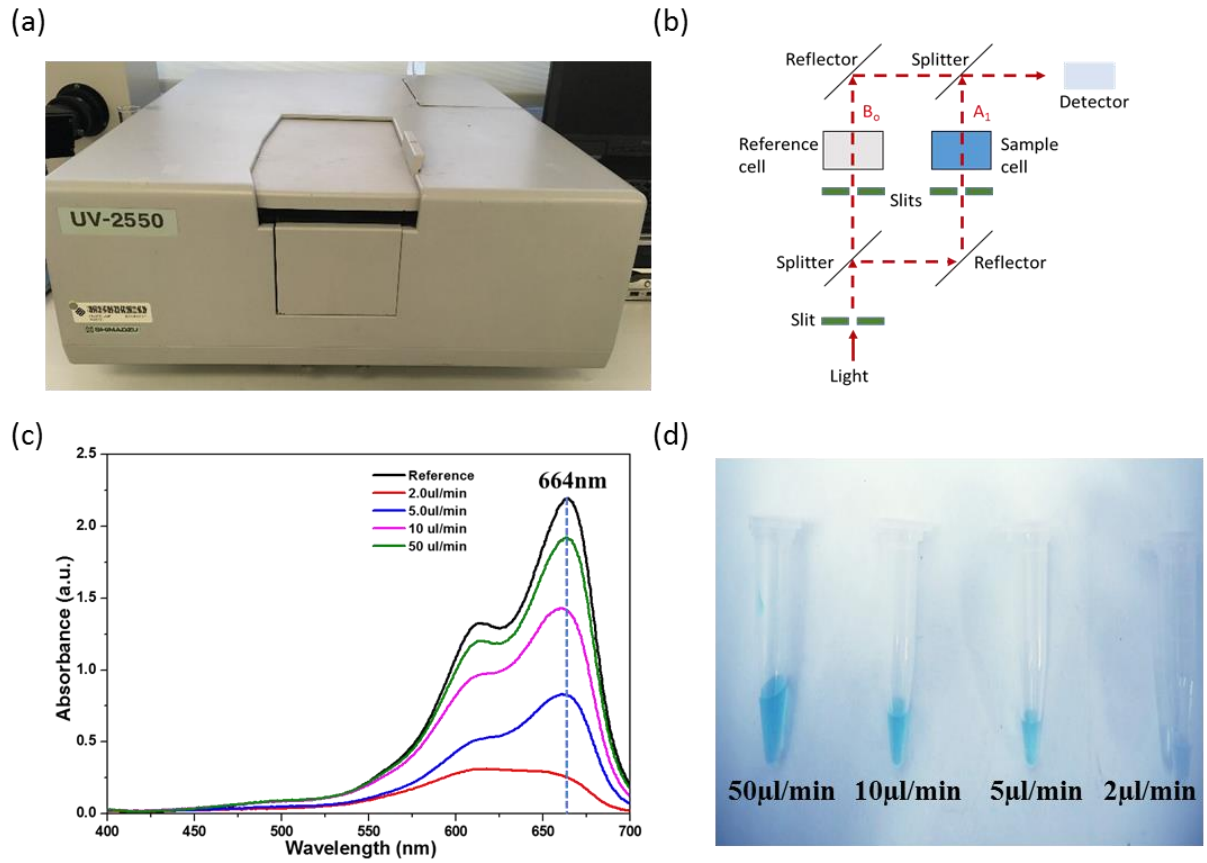

Figure 5.5 (a) Shimadzu UV-2550 UV-Visible Spectrometer makes use of quantitative way to determine the concentration of analytes. (b) The detection mechanism of the photo-spectrometer. (c) The measured absorption spectra of the MB solution at different flow rates. The characteristic

peak of MB remains at 664 nm, however the peak height drops at slower flow rate. (d) Photographs of the MB solutions, showing a color change from blue to very light blue when the flow rate drops from 50 μm/min to 2 μm/min.

Before the measurement of the absorption spectra of TiO_2 and Au/TiO_2, the as-prepared suspensions were rolled to form thin films on the glass substrate. **Figure 5.6** shows the absorption spectra. The literature data [85, 86] are shown in **Figure 5.6(a)** for reference purpose, showing a broad plasmonic peak in 475-600 nm. The absorption spectra of our prepared TiO_2 and Au/TiO_2 are plotted in **Figure 5.6(b)**. For TiO_2, the absorption is flat and low over the range of 400-700 nm. For Au/TiO_2, much enhanced absorption appears, with the peak over 500-600 nm. This well agrees with the literature data [85, 86].

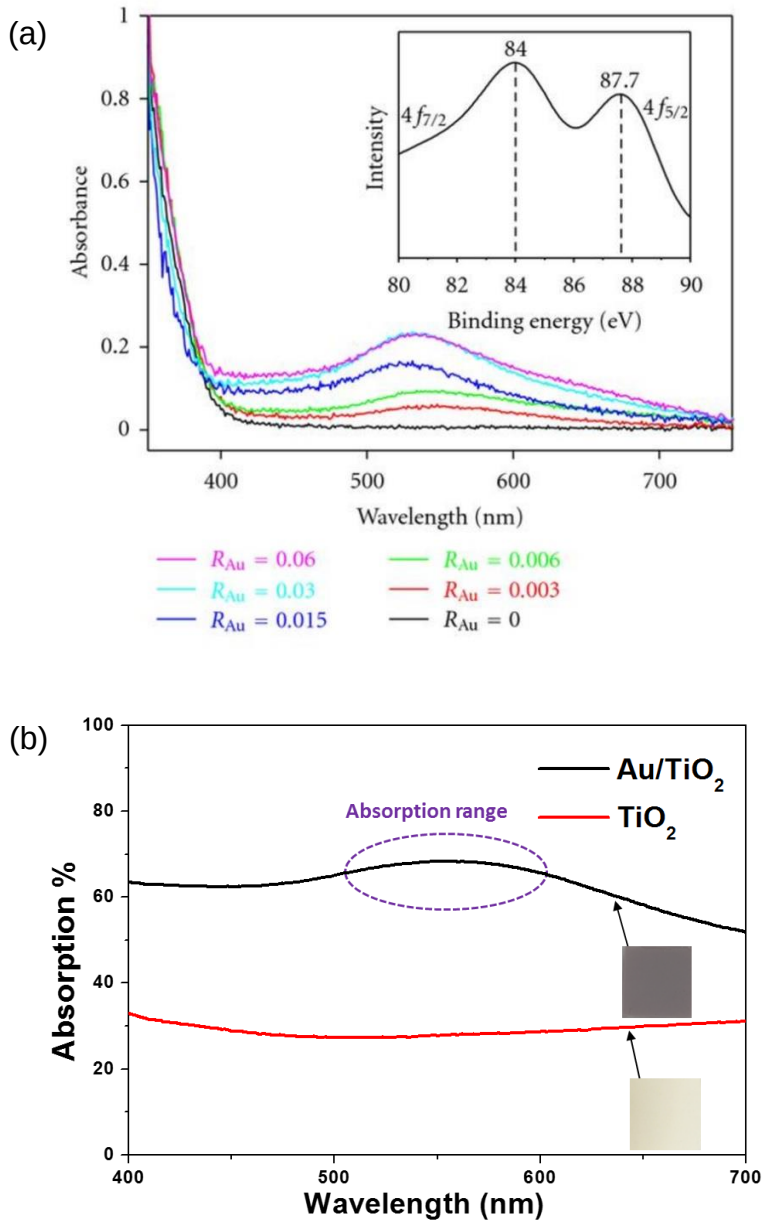

Figure 5.6 (a) The upper graph shows the literature data of UV-Vis absorption spectra of Au/TiO_2 composite powders with different radii (measured in μm) of Au. From the graph, Au/TiO_2 absorbs from 475nm to 600nm [84, 85]. (b) Photocatalyst film on the glass substrate was tested by integrated sphere, there was absorption range from 500nm to 600nm (indicated by purple dash line). The result of (a) and (b) was consistent with each other.

5.4 Transmission of stuffed-mode microfluidic reactor

The choice of the thickness of photocatalysts (i.e., TiO_2 or Au/TiO_2) layer- is important for the performance comparison. First, the photocatalyst layer should be thick enough to absorb and utilize most of the incident light. Second, the photocatalyst layer in the stuffed-mode microfluidic reactor cannot be too high. Otherwise, the photocatalyst microspheres at the bottom part receive no light and do not participate in the photodegradation, causing something like a leakage of the not-degraded MB solution and thus deteriorating the overall photodegradation efficiency. Finally, to make a fair comparison of the efficiency of different photocatalysts (TiO_2 or Au/TiO_2) in different microfluidic reactors (film-mode or stuffed-mode), we should ensure the absorption is at the same level.

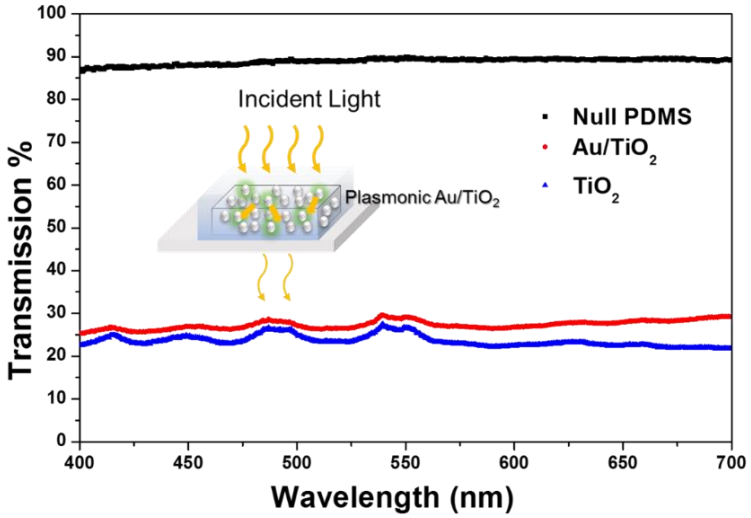

Figure 5.7 Measured transmission of the whole stuffed-mode microfluidic reactor. Most of the light can penetrate PDMS, while light transmission has an attenuation through the vertical profile of the chamber. Still, at the bottom TiO_2 and Au/TiO_2 microfluidic reactor would retain 25% to

30% light intensity after light penetrates through all particles inside. The slight fluctuation of the curves may be attributed to the roughness of the PDMS surface.

A simple method to see whether the photocatalyst thickness is appropriate is to measure the transmission percentage from the top of the microfluidic reactor to the bottom layer of particles. **Figure 5.7** shows how much light can pass through the entire device.

Stuffed particles in the microfluidic reactor scatter light in different directions [86], the attenuation of the light intensity is acceptable if the bottom layer of particles inside the stuffed-mode microfluidic reactor could be also utilized under light. Another way to ensure fair comparison of different photocatalysts (TiO_2 or Au/TiO_2) is to repeated use the same microfluidic reactor. Of course, thorough rinsing and dark adsorption saturation are involved before each reuse of reactor.

5.5 Action spectrum of photocatalysts in microfluidic reactor

To verify the LSPR enhancement, the action spectrum [87] was then measured for the stuffed-mode microfluidic reactor filled with photocatalysts. For this purpose, the photodegradation per photon flux density is determined against different monochromatic lights of xenon light source. Here the flow rate is fixed at 20 μm/min.

The incident photons to photodegradation efficiency (i.e., photodegradation quantum efficiency η) is used to indicate how efficiency each photon at a specific wavelength would contribute to photodegradation [88]. It is defined as follows:

$$n_p = \frac{P\lambda}{hc} \qquad \textbf{(5.1a)}$$

$$n_{MB} = \frac{(c_0 - c)V_0 N_A}{t_r} \quad \textbf{(5.1b)}$$

$$\eta = \frac{n_{MB}}{n_p} = \frac{hcN_A(c_0 - c)V_0}{Pt_r\lambda} = \frac{hcN_A(c_0 - c)Q}{P\lambda} \quad \textbf{(5.2)}$$

where n_p is the number of incident photons per unit time, P is the power of the incident light detected, h is the Planck constant, c is a speed of light in vacuum, N_A is the Avogadro constant, V_0 is the volume of reaction chamber, t_r is the residence time, $Q=V_0/t_r$ is the flow rate. The physical meaning of η is that how many MB molecoles are degraded by each incident photon, like the external quantum efficiency. It is noted from **Equation (5.2)** that η is inversely proportional to λ.

Figure 5.8 shows there is a prominent degradation peak from 500 to 600 nm [89] for Au/TiO_2, which the measured efficiency consists with the LSPR absorption peak in **Figure 5.6(b)**. This well proves that the LSPR effect enhances the photodegradation efficiency in the visible light range.

The same experiment was done for TiO_2, which acts as the control experiment. The result is plotted in **Figure 5.9**. It is observed that TiO_2 does not show any peaks in the range from 500 nm to 600 nm. Besides, the photodegradation efficiency of each point for TiO_2 is always lower than that for Au/TiO_2. This further proves that Au/TiO_2 has better photodegradation performance in the stuffed-mode microfluidic reactor than TiO_2.

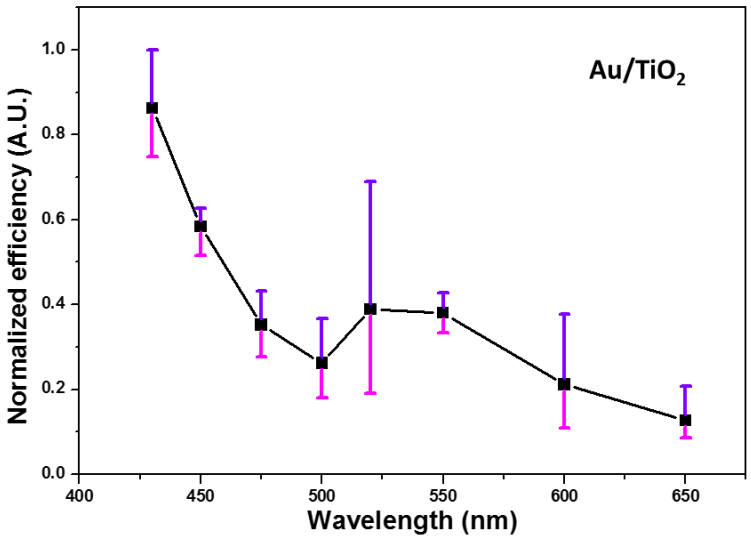

Figure 5.8 Photodegradation efficiency vs. wavelength is plotted for the action spectrum of Au/TiO_2 as measured in the stuffed-mode microfluidic reactor. A peak appears from 500 nm to 600 nm. Repeatability experiment of each point shows mean value and the deviation of extremes to the mean.

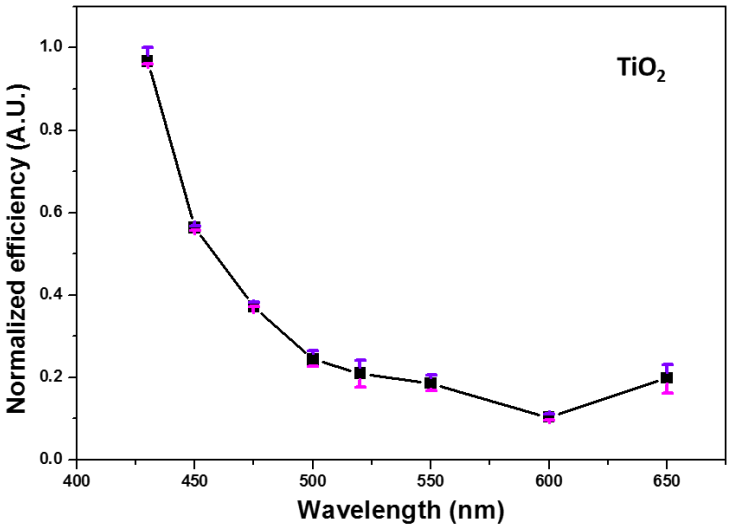

Figure 5.9 Action spectrum of TiO_2 as measured using the stuffed-mode microfluidic reactor. No peak appears in the visible light region.

5.6 Experimental result of suspension-mode microfluidic reactor

Before the irradiation of light onto the mixture containing the MB solution and photocatalyst, the container was kept in darkness until the complete saturation between MB molecules and photocatalyst particles. It can be quantitatively found by measuring the concentration of the MB solutions collected at specific 15-min interval, as shown in **Figure 5.10**. Since the suspension mixture was stirred to increase the rate of adsorption of MB molecules on the surface of photocatalyst particles, it takes less time (~20 – 30 mins) to reach the adsorption saturation.

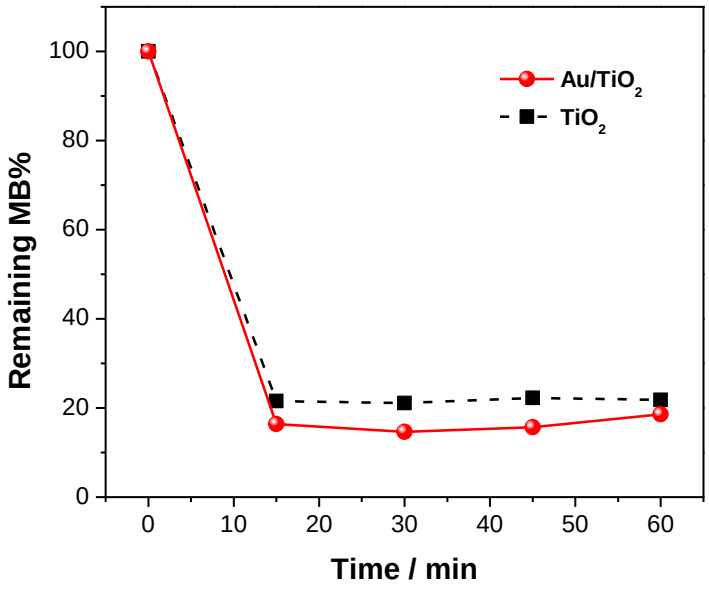

Figure 5.10 The adsorption efficiency of Au/TiO_2 and TiO_2 in the containers. It takes least time (~20 – 30 mins) for the adsorption saturation among different modes (i.e., the film-mode microfluidic reactor and the stuffed-mode microfluidic reactor).

5.6.1 Photodegradation efficiency

Suspension mode reactor is the first and simple experiments for the performance comparison of photocatalytic materials. Herein, the reaction time is defined as the time taken to collect the sample from the container. It is seen from **Figure 5.11** that Au/TiO_2 can have 45 times more efficient photodegradation performance than TiO_2 since the slope of the curve for Au/TiO_2 is larger than that for TiO_2.

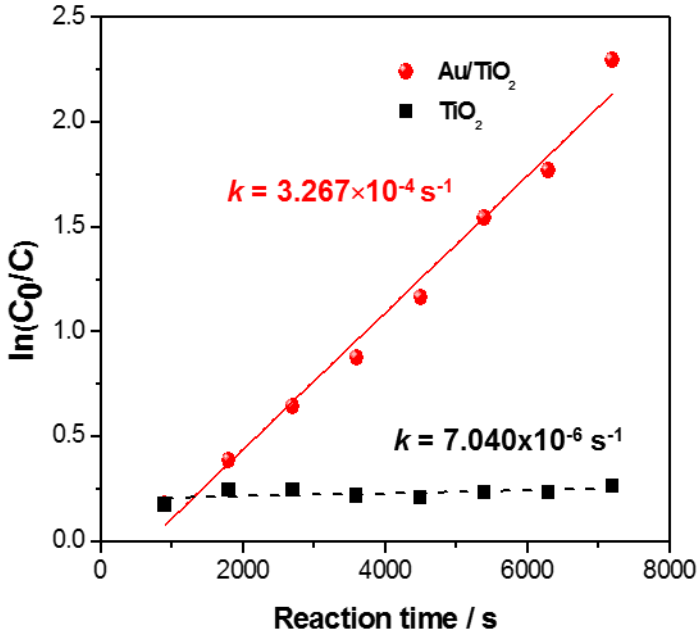

Figure 5.11 The photodegradation efficiency of TiO_2 and Au/TiO_2 in the suspension-mode microfluidic reactor. It shows that Au/TiO_2 is more efficient to photodegrade the MB solution than TiO_2.

5.7 Experimental result of film-mode microfluidic reactor

In the experiment procedure, dark reaction needs to be carried out before light reaction. This is crucial for MB to adhere to the surface of the photocatalyst particles because the reaction rate is dependent on the number of MB molecules attached to photocatalyst particles. Absorption spectrum is to find out how long it takes for MB to be saturated on the photocatalyst particles. **Figure 5.12** shows the time dependence of the remaining MB in the dark reaction for the film-mode microfluidic reactor. The MB solution after passing the film-mode microfluidic reactor is sampled at every 15-minute interval, and the concentration of MB is measured and compared with the initial MB concentration. **Figure 5.12** shows that it takes a relatively long time (~40 minutes) for complete dark reaction. Since the MB solution pumping into the chamber flows more smoothly than that in the stuffed-mode microfluidic reactor, it needs more time for MB to move downwards for adhesion to the photocatalyst particles. This is related to the diffusion length.

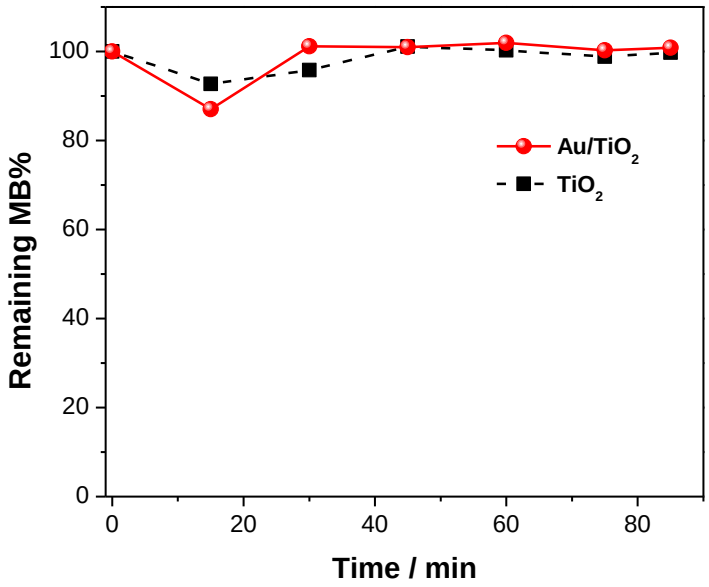

Figure 5.12 The absorption efficiency of MB against time (in minute) in the film-mode microfluidic reactor in dark reaction. It took less than one hour for observable equilibrium.

5.7.1 Photodegradation efficiency

The popular method for rapid test is to utilize a uniform photocatalyst film deposited on the surface of the glass substrate to form a film-mode microfluidic reactor. For TiO_2 and Au/TiO_2, the results of photodegradation are plotted in **Figure 5.13**. The vertical axis is ln (C_0/C), which is proportional to *t* according to **Equation (3.13)**. Therefore, the slope of curve is the reaction rate constant. It can be seen from **Figure 5.13** that the slopes for Au/TiO_2 and TiO_2 are 0.00897 s^{-1} and 0.00283 s^{-1}, respectively. Au/TiO_2 is 3-fold more efficient than TiO_2 for photocatalysis in the film mode. It is also interesting to find that these two rate constants are higher than two corresponding rate constants obtained using the suspension-mode reactor (i.e., 7.04×10^{-6} for TiO_2 and 3.27×10^{-4} for Au/TiO_2) regardless of the sample size.

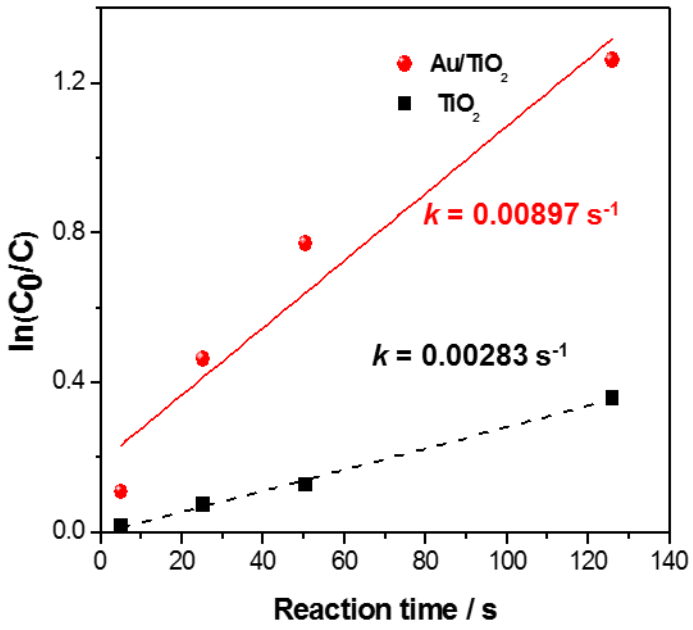

Figure 5.13 Photodegradation of MB solution using TiO_2 and Au/TiO_2 in the film-mode microfluidic reactor. The slope of curve represents the reaction rate constant. It is observed that Au/TiO_2 is 3 times more efficient than TiO_2 to degrade MB. The LSPR effect of Au/TiO_2 allows the absorption of more visible light and thus enhances the photocatalytic efficiency.

5.8 Experimental result of stuffed-mode microfluidic reactor

Like the film-mode microfluidic reactor, the stuffed-mode microfluidic reactor also needs to pump the MB solution into the chamber until the concentration of the MB at the outlet is nearly constant. After the saturation of adsorption, light reaction will be then carried out. Dark reaction in the stuffed-mode microfluidic reactor takes more time than that in the film-mode microfluidic reactor.

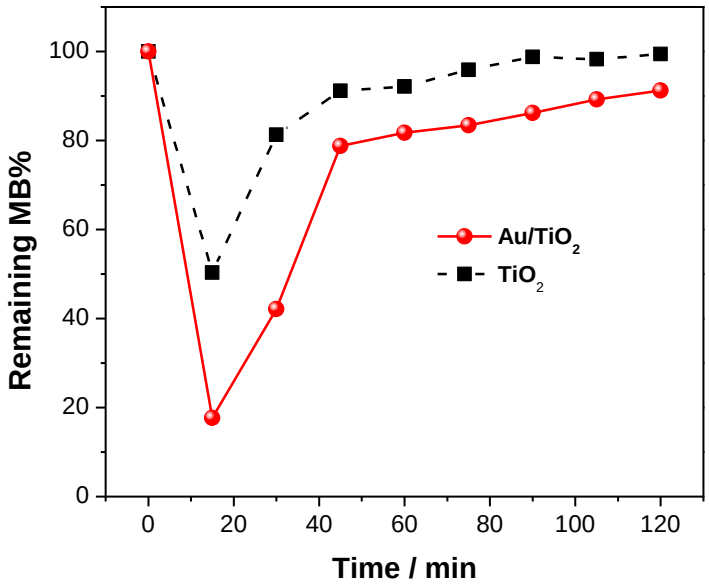

Figure 5.14 Adsorption time for the stuffed-mode microfluidic reactor is longer than the film-mode microfluidic reactor. It is reasonable because there are more adsorption sites for MB

From **Figure 5.14**, it shows that it takes more than 2 hours for dark reaction, much longer than the saturation time of 40 mins for the film-mode microfluidic reactor. This is reasonable since the stuffed-mode microfluidic reactor contains more photocatalyst particles and has more effective adsorption sites. It is consistent with the fact that the stuffed photocatalysts are packed inside the chamber. Although the diffusion length becomes shorter, MB still needs a longer time to adhere to more active sites of photocatalyst particles for light reaction.

5.8.1 Photodegradation efficiency

The measured photodegradation results are plotted in **Figure 5.15** for TiO_2 microspheres and Au/TiO_2 microspheres filled in the stuffed mode microfluidic reactor. The reaction rate constants evaluated from the slopes of the linear fittings are 0.02294 s^{-1} and 0.01289 s^{-1} for Au/TiO_2 and

TiO_2, respectively, showing an enhancement of 1.78. In the other word, Au/TiO_2 is nearly two-fold more efficient as TiO_2.

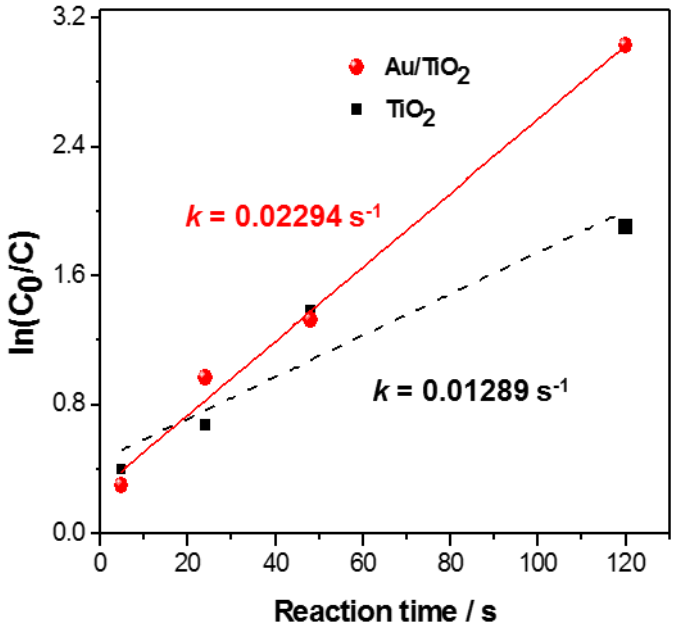

Figure 5.15 Photodegradation of MB using TiO_2 and Au/TiO_2 in the stuffed-mode microfluidic reactor. The slopes show that the photocatalytic efficiency for the stuffed-mode is greater than that for the film-mode because the rate constant is increased here. Au/TiO_2 in this mode has the steepest slope due to the LSPR enhanced absorption and the stuffed-mode enhanced SA:V.

5.8.2 Repeatability test

To further test the stability of TiO_2 microspheres and Au/TiO_2 microspheres in the stuffed-mode microfluidic reactor, each flow rate is tested for 3 times. Of course, thorough rinsing and saturated adsorption are conducted before photodegradation. The data are plotted in **Figure 5.16**. For control experiment, the microfluidic reactor without TiO_2 or Au/TiO_2 are also pumped with the MB

solution, which reflects the photolysis of MB. From **Figure 5.16**, Au/TiO_2 gives the highest rate constant of 0.0224 s^{-1} and relatively large deviation range in all data points; in contrast, TiO_2 yields 0.0108 s^{-1} and reduced deviation. For the photolysis of MB, it is 0.00148 s^{-1}, much smaller the previous two.

What we can conclude from the above test are:

(1) The photodegradation performances of TiO_2 and Au/TiO_2 in the stuffed-mode microfluidic reactor are repeatable, though not idea.

(2) Au/TiO_2 is about 2 times as efficient as TiO_2, matching the result in **Figure 5.15**.

(3) Photolysis of MB is small, though not negligible.

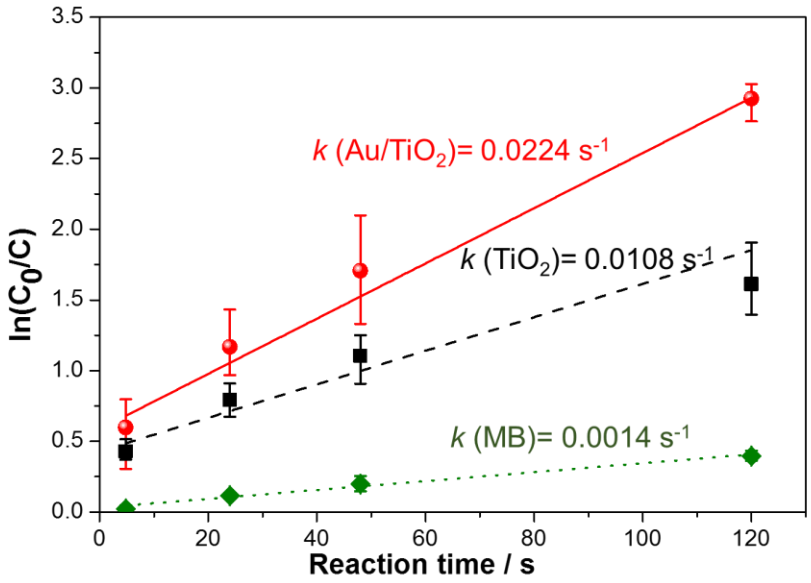

Figure 5.16 Repeatability test of photodegradation of TiO_2 and Au/TiO_2 using the stuffed-mode microfluidic reactor. It could be seen that linear fit of each material in the stuffed mode microfluidic reactor match the central point (mean of the three measurements) closely.

5.9 Comparison of stuffed-mode and film-mode

The photodegradation efficiencies of the stuffed-mode and the film-mode microfluidic reactor are compared in term of the rate constant as listed in **Table 5.1**. It is seen that the enhancement factor of Au/TiO_2 relative to TiO_2 is 3.2 in the film-mode and 2.1 in the stuffed-mode; and the stuffed mode is more efficient than the film-mode by a factor 3.8 for TiO_2 and 2.5 for Au/TiO_2, respectively. The biggest difference would occur between TiO_2 in the film-mode and Au/TiO_2 in the stuffed mode, the factor is $3.2\times2.5=8$ times.

Comparison of the photodegradation efficiencies of TiO_2 and Au/TiO_2 in the stuffed-mode, film-mode and suspension-mode.

Table 5.1 Comparison of the photodegradation efficiencies of TiO_2 and Au/TiO_2 in the stuffed-mode, film-mode and suspension-mode.

	Rate constant (s^{-1})			**Enhancement factor&&**
	Suspension	**Film**	**Stuffed**	**Stuffed / film**
TiO_2	7.04×10^{-6}	0.00283	0.0108	3.8
Au/TiO_2	3.27×10^{-4}	0.00897	0.0224	2.5
Enhancement factor&	46	3.2	2.1	---

&: The rate constant ratio of two materials in each mode.

&&: The rate constant ratio of two modes in each material.

Microfluidic reactors should be durable for repeated uses. In **Figure 5.17,** three consecutive cycles of photocatalysis using Au/TiO_2 and TiO_2 were conducted. The performance of each cycle was repeatable since the linear relationship is maintained. In addition, the photodegradation

performance of the corresponding data point in each cycle declines insignificantly because photocatalyst particles may be flushed out in the repeated use.

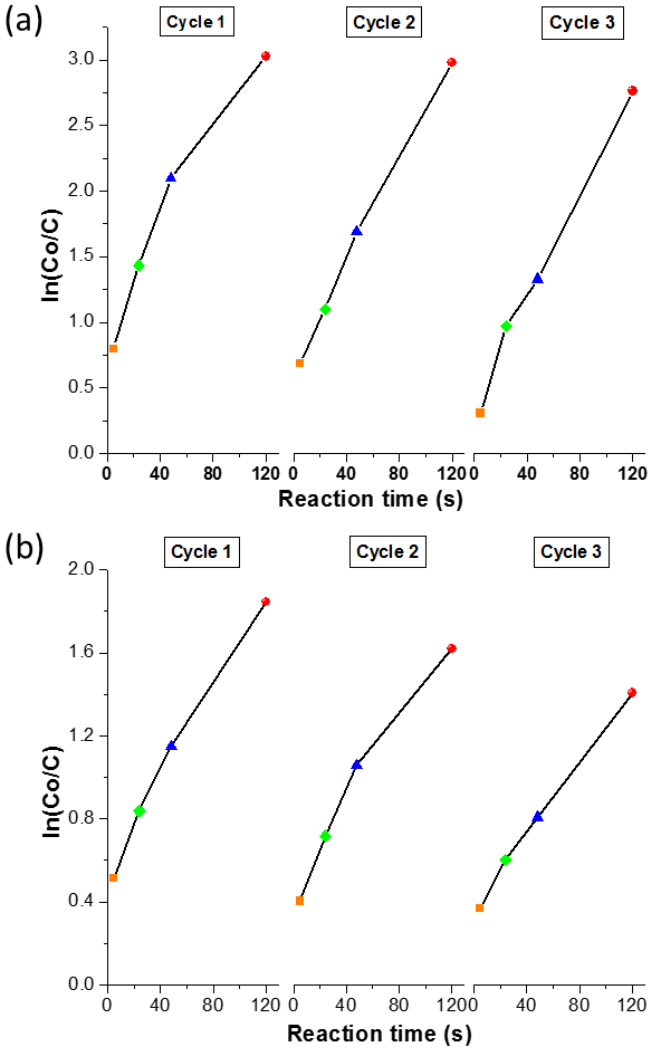

Figure 5.17 The three cycles of (a) Au/TiO_2 and (b) TiO_2 were conducted consecutively to show the durability of the device. The relationship ln (C_0/C) against reaction time is still linear. Moreover, Au/TiO_2 seems to have a better durability than TiO_2 since the photodegradation efficiency decline insignificantly [50].

5.10 Summary

In this chapter, extensive experiments have been conducted to study the photodegradation performances of TiO_2 and Au/TiO_2 using the stuffed-mode microfluidic reactor and the film-mode microfluidic reactor. In the material characterization, it is found that for Au/TiO_2 the action spectrum (i.e., photodegradation quantum efficiency vs. wavelength) has a broad peak in 500 - 600 nm and well matches the LSPR absorption peak in the same wavelength range whereas for TiO_2 there is no such peak. This proves that the enhanced photocatalytic efficiency of Au/TiO_2 is a contribution from the LSPR effect of AuNPs. Moreover, detailed comparative studies have shown that Au/TiO_2 presents to have an enhancement factor of 2~3 times relative to TiO_2, and the stuffed-mode enables an enhancement factor of 2.5 - 4 with respective to the film-mode. The combination of Au/TiO_2 and the stuffed-mode would provide an enhancement by 8 times.

Chapter 6 Conclusion and Future Work

6.1 Conclusion

This research has focused on the enhancement of photocatalytic efficiency of water purification using visible light in two aspects: new plasmonic photocatalyst materials and new design of microfluidic reactors. In the former aspect, four material forms have been developed, including TiO_2 film, TiO_2 microsphere, Au/TiO_2 film and Au/TiO_2 microsphere. In the latter aspect, two modes of microfluidic reactors have been studied, including the film-mode and the stuffed-mode. Here the stuffed-mode microfluidic reactor is new and original. It is the first time that the chamber of microreactor is stuffed with TiO_2 or Au/TiO_2 microspheres to enhance the photocatalytic efficiency.

In this thesis, extensive studies have been conducted on the device designs, the performance simulation and analysis, the material preparation, the device fabrication, and the experimental characterization of the photocatalytic properties. By comparing the absorption spectrum of Au/TiO_2 and the active spectrum of Au/TiO_2 in microfluidic reactor, it is experimentally shown that the peaks of both spectra appear at the same wavelength range, proving that the plasmonic enhancement of LSPR to the photodegradation using visible light. The comparison of TiO_2 and Au/TiO_2 shows that Au/TiO_2 presents an enhancement factor of 2 – 3 times; and another comparative study has shown that the stuffed mode enables an enhancement factor of 2.5 – 4 times. The combined use of Au/TiO_2 and the stuffed mode together produces an enhancement factor of 8 times. In the long run, the microfluidic devices should be scaled up [90, 91] to handle massive sewage water.

6.2 Future work

The research of this M.Phil. study leaves plenty of room to improve and to pursue further. Some prominent aspects are presented as follows:

(1) Uniform packing of particles in the microfluidic reactor: The packing state is critical to the SA:V ratio, however, it is often a random process. To ensure a uniform packing of Au/TiO_2 and TiO_2 in the stuffed-mode microfluidic reactors, optical microscope cab be used to check the immobilized pattern before and after drying out of the solvent that carries the photocatalyst microspheres. To make a more controllable and robust stuffed-mode microfluidic reactor, the photocatalyst microspheres may be arrayed on the glass slide and stacked layer by layer by the hydrothermal synthesis before the PDMS slab is capped. Normally, this method ensures that materials could not be easily flushed away by the pumping MB. Besides, it ensures high accuracy of the prepared photocatalysts sample, which make data more controllable and convincing. However, clogging may occur in the tube that is connected to the outlet of microfluidic reactor.

(2) New photolithographic patterns: The pattern used in this research is easy and relatively stable for fluidic flow because of symmetry and micro-capillary channel. The chamber is used to immobilize photocatalyst microparticles. This is simple and easy to achieve since only one phase (i.e., liquid phase) is needed for the photocatalytic reaction. In some situations, more patterns and inlets/outlets may be needed [92], for instance, complex patterns may be needed to separate several reaction chambers for individual reaction. In another example, fluidized-bed reactor may be developed, which involves two phases (i.e., liquid and solid) in the

microfluidic reactor: the indicator solution and the solid catalysts. These two could be injected together into the chamber by two inlets.

(3) Use of other dyes as the indicator: Methylene blue (MB) is commonly used to study the photocatalytic efficiency. Its chemical kinetics in photocatalysis are well investigated. However, MB has the absorption peak at 664 nm. Under the irradiation of sunlight, it is and is subject to photolysis, which is not negligible [93]. Besides, MB may also sensitize the photocatalyst like TiO_2, making the analysis complicated. To avoid these drawbacks, it is possible to use other indicator solutions that have the absorption peak in other regions such as UV or infrared.

(4) Scaling up the microfluidic reactor for mass process: The microfluidic reactor can process only very small volume of water sample per unit time (typically 1 μl/min) but the real application of water purification needs to deal with large amount of water (e.g., 1,000 ton/hour). It is necessary to study how to scale up the microfluidic reactor to the large reactor [26]. However, the microfluidic reactor is a proof-of-concept device which displays the photodegradation performance of plasmonic materials assisted with a small chip and solar light.

The items listed above are only a few examples of many specific topics for further study. More work may also be worth investigation, like the integration of the microfluidic reactor with other functional parts (e.g., on-chip spectrometer for in-line real-time monitoring), the application of the microfluidic reactors to other research fields (e.g., photosynthesis, bio-enzymatic reactions), etc. There are plenty of topics for further study. Imagination is the only limit.

Nomenclature

A and B:	Ergun constant	U:	Superficial velocity packed bed
ΔP:	Pressure change between two ends	Q:	Discharge rate (m^3/s)
q :	The discharge per area (m/s)	K:	Permeability of the medium (m^2)
A:	Cross-sectional area (m^2)	μ:	Dynamic viscosity (Pa·s)
f :	Fanning friction factor	ε:	Void fraction of the bed
D_p:	Diameter of particle (m)	L:	Bed length (m)
$P_2 - P_1$:	Pressure difference of two ends (Pa)	Re_f :	Reynolds number for film mode
Re:	Reynolds number	C:	Fanning coefficient
Re_p:	Reynolds number for packed mode	V_s:	Superficial velocity
ρ:	Fluid density	D_h:	Hydraulic diameter

Reference

[1] M. N. Chong, B. Jin, C. W. K. Chow, and C. Saint, "Recent developments in photocatalytic water treatment technology: A review," *Water Research*, vol. 44, pp. 2997-3027, 2010/05/01/ 2010.

[2] S. Padikkaparambil, B. Narayanan, Z. Yaakob, S. Viswanathan, and S. M. Tasirin, "Au/TiO2 reusable photocatalysts for dye degradation," *International Journal of Photoenergy*, vol. 2013, pp. 10, 2013.

[3] J.-M. Herrmann, "Heterogeneous photocatalysis: fundamentals and applications to the removal of various types of aqueous pollutants," *Catalysis Today*, vol. 53, pp. 115-129, 1999.

[4] D. Sinton, "Energy: the microfluidic frontier," *Lab on a Chip*, vol. 14, pp. 3127-3134, 2014.

[5] G. M. Whitesides, "The origins and the future of microfluidics," *Nature*, vol. 442, pp. 368, 2006.

[6] S. Yujun, H. Josef, and K. C. S. S. R., "Microfluidic synthesis of nanomaterials," *Small*, vol. 4, pp. 698-711, 2008.

[7] H. Xu, S. Ouyang, L. Liu, P. Reunchan, N. Umezawa, and J. Ye, "Recent advances in TiO2-based photocatalysis," *Journal of Materials Chemistry A*, vol. 2, pp. 12642-12661, 2014.

[8] Z. Xuming, C. Yu Lim, L. Ru-Shi, and T. Din Ping, "Plasmonic photocatalysis," *Reports on Progress in Physics*, vol. 76, pp. 046401, 2013.

[9] A. L. Linsebigler, G. Lu, and J. T. Yates, "Photocatalysis on TiO_2 surfaces: Principles, Mechanisms, and Selected Results," *Chemical Reviews,* vol. 95, pp. 735-758, 1995.

[10] T. Hirakawa and Y. Nosaka, "Properties of $O_2^{\bullet-}$ and $OH^{\bullet}$ formed in TiO_2 aqueous suspensions by photocatalytic reaction and the influence of H_2O_2 and some ions," *Langmuir,* vol. 18, pp. 3247-3254, 2002.

[11] N. Wang, X. Zhang, Y. Wang, W. Yu, and H. L. W. Chan, "Microfluidic reactors for photocatalytic water purification," *Lab on a Chip,* vol. 14, pp. 1074-1082, 2014.

[12] S. S. S., H. M. J., B. Jean-François, and G. Alain, "Visible-light photocatalysis in titania-based mesoporous thin films," *Advanced Materials,* vol. 20, pp. 1493-1498, 2008.

[13] J. Ryu and W. Choi, "Substrate-specific photocatalytic activities of TiO_2 and multiactivity test for water treatment application," *Environmental Science & Technology,* vol. 42, pp. 294-300, 2008.

[14] M. A. Fox and M. T. Dulay, "Heterogeneous photocatalysis," *Chemical Reviews,* vol. 93, pp. 341-357, 1993.

[15] O. Ola and M. M. Maroto-Valer, "Review of material design and reactor engineering on TiO_2 photocatalysis for CO_2 reduction," *Journal of Photochemistry and Photobiology C: Photochemistry Reviews,* vol. 24, pp. 16-42, 2015.

[16] B. J. Morgan and G. W. Watson, "Intrinsic n-type defect formation in TiO_2: A comparison of rutile and anatase from GGA+U calculations," *The Journal of Physical Chemistry C,* vol. 114, pp. 2321-2328, 2010.

[17] Y. Shiraishi, N. Yasumoto, J. Imai, H. Sakamoto, S. Tanaka, S. Ichikawa, *et al.*, "Quantum tunneling injection of hot electrons in Au/TiO2 plasmonic photocatalysts," *Nanoscale,* vol. 9, pp. 8349-8361, 2017.

[18] M. R. Khan, T. W. Chuan, A. Yousuf, M. N. K. Chowdhury, and C. K. Cheng, "Schottky barrier and surface plasmonic resonance phenomena towards the photocatalytic reaction: study of their mechanisms to enhance photocatalytic activity," *Catalysis Science & Technology,* vol. 5, pp. 2522-2531, 2015.

[19] L. Lei, N. Wang, X. M. Zhang, Q. Tai, D. P. Tsai, and H. L. W. Chan, "Optofluidic planar reactors for photocatalytic water treatment using solar energy," *Biomicrofluidics,* vol. 4, pp. 043004, 2010.

[20] X. Li, H. Wang, K. Inoue, M. Uehara, H. Nakamura, M. Miyazaki, *et al.*, "Modified micro-space using self-organized nanoparticles for reduction of methylene blue," *Chemical Communications,* pp. 964-965, 2003.

[21] M. M. Kearney, "Fractal device for mixing and reactor applications," ed: Google Patents, 2004.

[22] X. Chen, T. Li, J. Shen, and Z. Hu, "Fractal design of microfluidics and nanofluidics—A review," *Chemometrics and Intelligent Laboratory Systems,* vol. 155, pp. 19-25, 2016.

[23] R. S. Subramanian, "Flow through packed beds and fluidized beds," *URL: http://www. pdfdrive.com/flow-through-packed-bedsand-fluidized-beds-clarkson-university-e1826488. html,* 2004.

[24] L. Theodore, *Chemical reactor analysis and applications for the practicing engineer* vol. 5: John Wiley & Sons, 2012.

[25] P. Fernández-Ibáñez, J. Blanco, S. Malato, and F. J. d. l. Nieves, "Application of the colloidal stability of TiO_2 particles for recovery and reuse in solar photocatalysis," *Water Research,* vol. 37, pp. 3180-3188, 2003.

[26] K. F. Jensen, "Microreaction engineering — is small better?," *Chemical Engineering Science,* vol. 56, pp. 293-303, 2001.

[27] D. Nemec and J. Levec, "Flow through packed bed reactors: 1. Single-phase flow," *Chemical Engineering Science,* vol. 60, pp. 6947-6957, 2005.

[28] L. Henrik, W. Robert, and I. Alexander, "High surface area titania photocatalytic microfluidic reactors," *AIChE Journal,* vol. 53, pp. 695-702, 2007.

[29] J. Parmar, S. Jang, L. Soler, D.-P. Kim, and S. Sanchez, "Nano-photocatalysts in microfluidics, energy conversion and environmental applications," *Lab on a Chip,* vol. 15, pp. 2352-2356, 2015.

[30] S. G. Kandlikar, D. Schmitt, A. L. Carrano, and J. B. Taylor, "Characterization of surface roughness effects on pressure drop in single-phase flow in minichannels," *Physics of Fluids,* vol. 17, pp. 100606, 2005.

[31] D. J. Schmitt, "Experimental investigation of surface roughness microstructures and their effects on pressure drop characteristics in rectangular minichannels," 2004.

[32] M. J. Baker, "CFD simulation of flow through packed beds using the finite volume technique," 2011.

[33] S. Middleman, *An introduction to fluid dynamics: principles of analysis and design*: Wiley New York:, 1998.

[34] M. W. Losey, M. A. Schmidt, and K. F. Jensen, "Microfabricated multiphase packed-bed reactors: characterization of mass transfer and reactions," *Industrial & Engineering Chemistry Research,* vol. 40, pp. 2555-2562, 2001.

[35] S. Corbel, N. Becheikh, T. Roques-Carmes, and O. Zahraa, "Mass transfer measurements and modeling in a microchannel photocatalytic reactor," *Chemical Engineering Research and Design,* vol. 92, pp. 657-662, 2014.

[36] K. Ma, R. Liontas, C. A. Conn, G. J. Hirasaki, and S. L. Biswal, "Visualization of improved sweep with foam in heterogeneous porous media using microfluidics," *Soft Matter,* vol. 8, pp. 10669-10675, 2012.

[37] H. Wenbo and C. S. B., "A review of surface plasmon resonance-enhanced photocatalysis," *Advanced Functional Materials,* vol. 23, pp. 1612-1619, 2013.

[38] H. Li, Z. Li, Y. Yu, Y. Ma, W. Yang, F. Wang, *et al.*, "Surface-plasmon-resonance-enhanced photoelectrochemical water splitting from Au-nanoparticle-decorated 3D TiO_2 nanorod architectures," *The Journal of Physical Chemistry C,* vol. 121, pp. 12071-12079, 2017.

[39] A. A. Madhavan, G. G. Kumar, S. Kalluri, J. Joseph, S. Nagarajan, S. Nair, *et al.*, "Effect of embedded plasmonic Au nanoparticles on photocatalysis of electrospun TiO_2 nanofibers," *Journal of Nanoscience and Nanotechnology,* vol. 12, pp. 7963-7967, 2012.

[40] S. Helen, T. J. D., and I. R. F., "A microfluidic system for controlling reaction networks in time," *Angewandte Chemie,* vol. 115, pp. 792-796, 2003.

[41] L. Li, R. Chen, X. Zhu, H. Wang, Y. Wang, Q. Liao, *et al.*, "Optofluidic microreactors with TiO_2-coated fiberglass," *ACS Applied Materials & Interfaces,* vol. 5, pp. 12548-12553, 2013.

[42] W. Liao, N. Wang, T. Wang, J. Xu, X. Han, Z. Liu, *et al.*, "Biomimetic microchannels of planar reactors for optimized photocatalytic efficiency of water purification," *Biomicrofluidics,* vol. 10, pp. 014123, 2016.

[43] N. O. Mainya, P. Tum, and T. M. Muthoka, "Photodegradation and adsorption of methyl orange and methylene blue dyes on TiO_2," *Int. J. Sci. Res,* vol. 4, pp. 3185-3189, 2013.

[44] N. Wang, F. Tan, Y. Zhao, C. C. Tsoi, X. Fan, W. Yu, *et al.*, "Optofluidic UV-Vis spectrophotometer for online monitoring of photocatalytic reactions," *Scientific Reports,* vol. 6, pp. 28928, 2016.

[45] L. Kocsis, P. Herman, and A. Eke, "The modified Beer–Lambert law revisited," *Physics in Medicine & Biology,* vol. 51, pp. N91, 2006.

[46] C.-H. Wu and J.-M. Chern, "Kinetics of photocatalytic decomposition of methylene blue," *Industrial & Engineering Chemistry Research,* vol. 45, pp. 6450-6457, 2006.

[47] S. Das and V. C. Srivastava, "Microfluidic-based photocatalytic microreactor for environmental application: a review of fabrication substrates and techniques, and operating parameters," *Photochemical & Photobiological Sciences,* vol. 15, pp. 714-730, 2016.

[48] C. Anderson and A. J. Bard, "An improved photocatalyst of TiO_2/SiO_2 prepared by a sol-gel synthesis," *The Journal of Physical Chemistry,* vol. 99, pp. 9882-9885, 1995.

[49] M. A. Rauf, M. A. Meetani, A. Khaleel, and A. Ahmed, "Photocatalytic degradation of methylene blue using a mixed catalyst and product analysis by LC/MS," *Chemical Engineering Journal,* vol. 157, pp. 373-378, 2010.

[50] A. Lamberti, "Microfluidic photocatalytic device exploiting PDMS/TiO_2 nanocomposite," *Applied Surface Science,* vol. 335, pp. 50-54, 2015.

[51] M. B. Kerby, R. S. Legge, and A. Tripathi, "Measurements of kinetic parameters in a microfluidic reactor," *Analytical Chemistry,* vol. 78, pp. 8273-8280, 2006.

[52] J. Yu, L. Yue, S. Liu, B. Huang, and X. Zhang, "Hydrothermal preparation and photocatalytic activity of mesoporous Au–TiO_2 nanocomposite microspheres," *Journal of Colloid and Interface Science,* vol. 334, pp. 58-64, 2009.

[53] S. S. K. and W. G. M., "Microfluidic devices fabricated in poly(dimethylsiloxane) for biological studies," *ELECTROPHORESIS,* vol. 24, pp. 3563-3576, 2003.

[54] L. C.-K. Liau, W.-W. Chou, and R.-K. Wu, "Photocatalytic lithography processing via poly(vinyl butyral)/TiO_2 photoresists by ultraviolet (UV) exposure," *Industrial & Engineering Chemistry Research,* vol. 47, pp. 2273-2278, 2008.

[55] J. Friend and L. Yeo, "Fabrication of microfluidic devices using polydimethylsiloxane," *Biomicrofluidics,* vol. 4, pp. 026502, 2010.

[56] S. Bhattacharya, A. Datta, J. M. Berg, and S. Gangopadhyay, "Studies on surface wettability of poly(dimethyl) siloxane (PDMS) and glass under oxygen-plasma treatment and correlation with bond strength," *Journal of Microelectromechanical Systems,* vol. 14, pp. 590-597, 2005.

[57] J. R. Anderson, "Fabrication of microfluidic systems in poly (dimethylsiloxane)," *Electrophoresis,* vol. 21, pp. 27-40, 2000.

[58] B. H. Jo, L. M. V. Lerberghe, K. M. Motsegood, and D. J. Beebe, "Three-dimensional micro-channel fabrication in polydimethylsiloxane (PDMS) elastomer," *Journal of Microelectromechanical Systems,* vol. 9, pp. 76-81, 2000.

[59] B. Ohtani, Y. Ogawa, and S.-i. Nishimoto, "Photocatalytic activity of amorphous−anatase mixture of titanium(IV) oxide particles suspended in aqueous solutions," *The Journal of Physical Chemistry B,* vol. 101, pp. 3746-3752, 1997.

[60] S. S. Al-Shamali, "Photocatalytic degradation of methylene blue in the presence of TiO_2 catalyst assisted solar radiation," *Australian Journal of Basic and Applied Sciences,* vol. 7, pp. 172-176, 2013.

[61] X. Z. Li and F. B. Li, "Study of Au/Au^{3+}-TiO_2 photocatalysts toward visible photooxidation for water and wastewater treatment," *Environmental Science & Technology,* vol. 35, pp. 2381-2387, 2001.

[62] N. Wang, L. Lei, X. M. Zhang, Y. H. Tsang, Y. Chen, and H. L. W. Chan, "A comparative study of preparation methods of nanoporous TiO_2 films for microfluidic photocatalysis," *Microelectronic Engineering,* vol. 88, pp. 2797-2799, 2011.

[63] H. Eskandarloo, A. Badiei, A. Tavakoli, and R. G. Lammertink, "A simple educational demonstration of fabrication and use of a photocatalytic microfluidic reactor," *Journal of Materials Education,* vol. 38, pp. 109-118, 2016.

[64] M. M. Khan, J. Lee, and M. H. Cho, "Au@TiO_2 nanocomposites for the catalytic degradation of methyl orange and methylene blue: An electron relay effect," *Journal of Industrial and Engineering Chemistry,* vol. 20, pp. 1584-1590, 2014.

[65] K. Min and Y. J. Yoo, "Recent progress in nanobiocatalysis for enzyme immobilization and its application," *Biotechnology and Bioprocess Engineering,* vol. 19, pp. 553-567, 2014.

[66] K. Meller, M. Szumski, and B. Buszewski, "Microfluidic reactors with immobilized enzymes—characterization, dividing, perspectives," *Sensors and Actuators B: Chemical,* vol. 244, pp. 84-106, 2017.

[67] S. H. Tan, N.-T. Nguyen, Y. C. Chua, and T. G. Kang, "Oxygen plasma treatment for reducing hydrophobicity of a sealed polydimethylsiloxane microchannel," *Biomicrofluidics,* vol. 4, pp. 032204, 2010.

[68] D. Bodas and C. Khan-Malek, "Hydrophilization and hydrophobic recovery of PDMS by oxygen plasma and chemical treatment—An SEM investigation," *Sensors and Actuators B: Chemical,* vol. 123, pp. 368-373, 2007.

[69] Z. Jinwen, E. A. Vera, and V. N. Hans, "Recent developments in PDMS surface modification for microfluidic devices," *ELECTROPHORESIS,* vol. 31, pp. 2-16, 2010.

[70] J. Schäffer, "Immobilization of TiO_2: Via different routes for photocatalytic reactions in a PDMS based microreactor," University of Twente, 2012.

[71] H. Yan, X. Wang, M. Yao, and X. Yao, "Band structure design of semiconductors for enhanced photocatalytic activity: The case of TiO_2," *Progress in Natural Science: Materials International,* vol. 23, pp. 402-407, 2013.

[72] K. Thamaphat, P. Limsuwan, and B. Ngotawornchai, "Phase characterization of TiO_2 powder by XRD and TEM," *Kasetsart J.(Nat. Sci.),* vol. 42, pp. 357-361, 2008.

[73] J. Yu, G. Wang, B. Cheng, and M. Zhou, "Effects of hydrothermal temperature and time on the photocatalytic activity and microstructures of bimodal mesoporous TiO_2 powders," *Applied Catalysis B: Environmental,* vol. 69, pp. 171-180, 2007.

[74] T. Luttrell, S. Halpegamage, J. Tao, A. Kramer, E. Sutter, and M. Batzill, "Why is anatase a better photocatalyst than rutile? - Model studies on epitaxial TiO_2 films," *Scientific Reports,* vol. 4, pp. 4043, 2014.

[75] J. Zhang, P. Zhou, J. Liu, and J. Yu, "New understanding of the difference of photocatalytic activity among anatase, rutile and brookite TiO_2," *Physical Chemistry Chemical Physics,* vol. 16, pp. 20382-20386, 2014.

[76] M. Murdoch, G. I. N. Waterhouse, M. A. Nadeem, J. B. Metson, M. A. Keane, R. F. Howe, *et al.*, "The effect of gold loading and particle size on photocatalytic hydrogen production from ethanol over Au/TiO2 nanoparticles," *Nature Chemistry,* vol. 3, pp. 489, 2011.

[77] H. Li, Z. Bian, J. Zhu, Y. Huo, H. Li, and Y. Lu, "Mesoporous Au/TiO_2 nanocomposites with enhanced photocatalytic activity," *Journal of the American Chemical Society,* vol. 129, pp. 4538-4539, 2007.

[78] D. S. Kim and S.-Y. Kwak, "The hydrothermal synthesis of mesoporous TiO_2 with high crystallinity, thermal stability, large surface area, and enhanced photocatalytic activity," *Applied Catalysis A: General,* vol. 323, pp. 110-118, 2007.

[79] K. Nakata and A. Fujishima, "TiO_2 photocatalysis: design and applications," *Journal of Photochemistry and Photobiology C: Photochemistry Reviews,* vol. 13, pp. 169-189, 2012.

[80] D. Erickson, D. Sinton, and D. Psaltis, "Optofluidics for energy applications," *Nature Photonics,* vol. 5, pp. 583, 2011.

[81] L. Du, A. Furube, K. Yamamoto, K. Hara, R. Katoh, and M. Tachiya, "Plasmon-Induced charge separation and recombination dynamics in gold−TiO_2 nanoparticle systems: dependence on TiO_2 particle size," *The Journal of Physical Chemistry C,* vol. 113, pp. 6454-6462, 2009.

[82] H. Förster, "UV/VIS spectroscopy," in *Characterization I: -/-*, H. G. Karge and J. Weitkamp, Eds., ed Berlin, Heidelberg: Springer Berlin Heidelberg, 2004, pp. 337-426.

[83] C. Yogi, K. Kojima, N. Wada, H. Tokumoto, T. Takai, T. Mizoguchi, *et al.*, "Photocatalytic degradation of methylene blue by TiO_2 film and Au particles-TiO_2 composite film," *Thin Solid Films*, vol. 516, pp. 5881-5884, 2008.

[84] M. Zhou, J. Zhang, B. Cheng, and H. Yu, "Enhancement of visible-light photocatalytic activity of mesoporous Au-TiO_2 nanocomposites by surface plasmon resonance," *International Journal of Photoenergy*, vol. 2012, pp. 10, 2012.

[85] I. Tanahashi, H. Iwagishi, and G. Chang, "Localized surface plasmon resonance sensing properties of photocatalytically prepared Au/TiO_2 films," *Materials Letters*, vol. 62, pp. 2714-2716, 2008.

[86] Z. Wang, J. El-Ali, M. Engelund, T. Gotsaed, I. R. Perch-Nielsen, K. B. Mogensen, *et al.*, "Measurements of scattered light on a microchip flow cytometer with integrated polymer based optical elements," *Lab on a Chip*, vol. 4, pp. 372-377, 2004.

[87] E. Kowalska, R. Abe, and B. Ohtani, "Visible light-induced photocatalytic reaction of gold-modified titanium(iv) oxide particles: action spectrum analysis," *Chemical Communications*, pp. 241-243, 2009.

[88] T. Van Gerven, G. Mul, J. Moulijn, and A. Stankiewicz, "A review of intensification of photocatalytic processes," *Chemical Engineering and Processing: Process Intensification*, vol. 46, pp. 781-789, 2007.

[89] A. Tanaka, S. Sakaguchi, K. Hashimoto, and H. Kominami, "Preparation of Au/TiO_2 with metal cocatalysts exhibiting strong surface plasmon resonance effective for photoinduced hydrogen formation under irradiation of visible light," *ACS Catalysis*, vol. 3, pp. 79-85, 2013.

[90] Y. Abdel-Maksoud, E. Imam, and A. Ramadan, "TiO_2 solar photocatalytic reactor systems: selection of reactor design for scale-up and commercialization—analytical review," *Catalysts*, vol. 6, pp. 138, 2016.

[91] V. S. Cabeza, "High and efficient production of nanomaterials by microfluidic reactor approaches," in *Advances in Microfluidics-New Applications in Biology, Energy, and Materials Sciences*, ed: InTech, 2016.

[92] J. C. McDonald and G. M. Whitesides, "Poly(dimethylsiloxane) as a material for fabricating microfluidic devices," *Accounts of Chemical Research*, vol. 35, pp. 491-499, 2002.

[93] X. Yan, T. Ohno, K. Nishijima, R. Abe, and B. Ohtani, "Is methylene blue an appropriate substrate for a photocatalytic activity test? A study with visible-light responsive titania," *Chemical Physics Letters*, vol. 429, pp. 606-610, 2006.